JGR Space Physics

RESEARCH ARTICLE
10.1029/2024JA033040

Key Points:

- Higher-order gravity waves (GWs) generated/amplified by the northern polar vortex jet create medium to large-scale traveling ionospheric disturbances (TIDs) with arc-like and planar structure
- Cross-polar higher-order GWs create daytime southward TIDs over North America which could be misidentified as being from geomagnetic forcing
- Higher-order GWs from the polar vortex jet may aid the formation of equatorial plasma bubbles over Africa and Brazil after sunset

Supporting Information:

Supporting Information may be found in the online version of this article.

Correspondence to:

S. L. Vadas,
vasha@nwra.com

Citation:

Vadas, S. L., Themens, D. R., Huba, J. D., Becker, E., Bossert, K., Goncharenko, L., et al. (2025). Higher-order gravity waves and traveling ionospheric disturbances from the polar vortex jet on 11–15 January 2016: Modeling with HIAMCM-SAMI3 and comparison with observations in the thermosphere and ionosphere. *Journal of Geophysical Research: Space Physics*, *130*, e2024JA033040. https://doi.org/10.1029/2024JA033040

Received 11 JUL 2024
Accepted 9 NOV 2024

Author Contributions:

Conceptualization: Sharon L. Vadas
Data curation: Sharon L. Vadas
Formal analysis: Sharon L. Vadas, David R. Themens, Katrina Bossert, Larisa Goncharenko, Sophie J. Maguire, Cosme A. O. B. Figueiredo, Shuang Xu, V. Lynn Harvey, Nathaniel A. Frissell, Michael J. Molzen, Thomas J. Pisano
Funding acquisition: Sharon L. Vadas
Investigation: Sharon L. Vadas, David R. Themens, Katrina Bossert, Larisa Goncharenko
Methodology: David R. Themens, Joseph D. Huba, Erich Becker, Katrina Bossert, Larisa Goncharenko, Sophie J. Maguire, Cosme A. O. B. Figueiredo, Shuang Xu,

Higher-Order Gravity Waves and Traveling Ionospheric Disturbances From the Polar Vortex Jet on 11–15 January 2016: Modeling With HIAMCM-SAMI3 and Comparison With Observations in the Thermosphere and Ionosphere

Sharon L. Vadas[1], David R. Themens[2], Joseph D. Huba[3], Erich Becker[1], Katrina Bossert[4,5,6], Larisa Goncharenko[7], Sophie J. Maguire[2], Cosme A. O. B. Figueiredo[8], Shuang Xu[9], V. Lynn Harvey[10], Nathaniel A. Frissell[11], Michael J. Molzen[11], Thomas J. Pisano[11], and Grzegorz Nykiel[12,13]

[1]Northwest Research Associates, Boulder, CO, USA, [2]University of Birmingham, Birmingham, UK, [3]Syntek Technologies, Fairfax, VA, USA, [4]Arizona State University, Tempe, AZ, USA, [5]School of Earth and Space Exploration, Arizona State University, Tempe, AZ, USA, [6]School of Mathematical and Statistical Sciences, Arizona State University, Tempe, AZ, USA, [7]Haystack Observatory, Massachusetts Institute of Technology, Westford, MA, USA, [8]Federal University of Campina Grande, UFCG, Campina Grande, Brazil, [9]Lawrence Livermore National Laboratory, Livermore, CA, USA, [10]Laboratory for Atmospheric and Space Physics, University of Colorado Boulder, Boulder, CO, USA, [11]Department of Physics and Engineering, University of Scranton, Scranton, PA, USA, [12]Institute for Solar-Terrestrial Physics, German Aerospace Center (DLR), Neustrelitz, Germany, [13]Civil and Environmental Engineering, Gdansk University of Technology, Gdansk, Poland

Abstract In Vadas et al. (2024, https://doi.org/10.1029/2024ja032521), we modeled the atmospheric gravity waves (GWs) during 11–14 January 2016 using the HIAMCM, and found that the polar vortex jet generates medium to large-scale, higher-order GWs in the thermosphere. In this paper, we model the traveling ionospheric disturbances (TIDs) generated by these GWs using the HIAMCM-SAMI3 and compare with ionospheric observations from ground-based Global Navigation Satellite System (GNSS) receivers, Incoherent Scatter Radars (ISR) and the Super Dual Auroral Radar Network (SuperDARN). We find that medium to large-scale TIDs are generated worldwide by the higher-order GWs from this event. Many of the TIDs over Europe and Asia have concentric ring/arc-like structure, and most of those over North/South America have planar wave structure and occur during the daytime. Those over North/South America propagate southward and are generated by higher-order GWs from Europe/Asia which propagate over the Arctic. These latter TIDs can be misidentified as arising from geomagnetic forcing. We find that the higher-order GWs that propagate to Africa and Brazil from Europe may aid in the formation of equatorial plasma bubbles (EPBs) there. We find that the simulated GWs, TIDs and EPBs agree with EISCAT, PFISR, GNSS, and SuperDARN measurements. We find that the higher-order GWs are concentrated at $60 - 90°$N at $z \geq 200$ km, in agreement with GOCE and CHAMP data. Thus the polar vortex jet is important for generating TIDs in the northern winter ionosphere via multi-step vertical coupling through GWs.

Plain Language Summary Gravity waves (GWs) are perturbations in the Earth's atmosphere. When a GW breaks, it imparts momentum and energy to the atmosphere. This deposition process unbalances the atmosphere, which in turn generates secondary GWs. The same process occurs at a higher altitude/horizontally displaced location for the secondary GWs, which results in the generation of higher-order GWs, etc. We simulate the primary, secondary and higher-order GWs and traveling ionospheric disturbances (TIDs) during 11–15 January 2016 using a GW-resolving global circulation model and an ionospheric model. We find that medium to large-scale TIDs are created by the higher-order GWs generated/amplified by the polar vortex jet. Many of the TIDs over Europe have concentric ring/arc-like structure. Some of the higher-order GWs from Europe propagate over the Arctic and generate TIDs that travel southward over North/South America during the daytime; such TIDs could be misidentified as arising from geomagnetic forcing. We also find that some of these GWs/TIDs may aid in the formation of equatorial plasma bubbles near South America and Africa. We find that the simulated TIDs and EPBs agree well with EISCAT, PFISR, GNSS and SuperDARN measurements. Thus the polar vortex jet is an important driver for generating TIDs in the Earth's ionosphere.

V. Lynn Harvey, Nathaniel A. Frissell, Michael J. Molzen, Thomas J. Pisano, Grzegorz Nykiel
Project administration: Sharon L. Vadas
Resources: Sharon L. Vadas
Supervision: Sharon L. Vadas, David R. Themens, Nathaniel A. Frissell
Validation: Sharon L. Vadas
Visualization: Sharon L. Vadas
Writing – original draft: Sharon L. Vadas
Writing – review & editing: Sharon L. Vadas, David R. Themens, Joseph D. Huba, Erich Becker, Katrina Bossert, Larisa Goncharenko, Cosme A. O. B. Figueiredo, Shuang Xu, V. Lynn Harvey, Nathaniel A. Frissell, Grzegorz Nykiel

1. Introduction

Primary GWs are generated by a variety of processes, including "spontaneous emission" from the core of the stratospheric polar vortex (e.g., Becker, Vadas, et al., 2022; O'Sullivan & Dunkerton, 1995; Plougonven & Zhang, 2014; Vadas, Becker, Bossert et al., 2023; Yoshiki & Sato, 2000). Here, energy is extracted from the vertical shear of the zonal and meridional neutral wind of the polar vortex jet to "fuel" the generated GWs (Becker, Vadas, et al., 2022). In addition, intrinsic westward GWs that propagate upward from below the polar vortex jet (e.g., mountain waves (MWs)) have increased vertical wavelengths $|\lambda_z|$ in the polar vortex jet (Alexander & Teitelbaum, 2007), thereby enabling them to propagate through most of the polar vortex jet before breaking (Vadas, Becker, Bossert et al., 2023) (hereafter V23).

GW breaking generates small-scale secondary GWs (e.g., Heale et al., 2022; Lund & Fritts, 2012). These GWs typically have small horizontal phase speeds, and therefore often do not propagate very far before being reabsorbed by the atmosphere; such GWs can be loosely thought of as being part of the transition to smaller scales and the cascade to turbulence. In addition, the localized deposition of momentum (called local body forces (LBFs)) and energy that results destabilizes the atmosphere; the atmosphere responds by generating a different type of secondary GWs which propagate upward and downward, have concentric ring structure, and have horizontal wavelengths ranging from a fraction to several times the horizontal extent of the GW packet (Vadas et al., 2003, 2018). The concentric ring structure of these latter GWs occurs because the LBFs and heatings are localized spatially. Note that constructive/destructive interference of primary GW packets from different sources can reduce the horizontal sizes of the LBFs and heatings (Vadas & Crowley, 2010), thereby reducing λ_H of the secondary GWs (Vadas & Becker, 2019). In this paper, secondary GWs refers to the GWs generated by the atmosphere's response to being unbalanced from momentum/energy deposition resulting from GW breaking and/or dissipation by molecular viscosity/ion drag. Those secondary GWs which travel upward propagate to higher altitudes at horizontally-displaced locations where they break/dissipate and deposit their momentum and energy into the atmosphere, thereby generating LBFs and heatings and unbalancing the atmosphere. The atmosphere responds by generating upward and downward-propagating, concentric higher-order GWs (Vadas & Becker, 2019). This cyclical process, called "multi-step vertical coupling" (MSVC), can occur multiple times at different altitudes and locations. In this paper, we use the terms secondary and higher-order GWs interchangeably. GWs generate traveling ionospheric disturbances (TIDs) in the ionosphere from the push and pull of plasma along the Earth's magnetic field via ion-neutral collisions (Djuth et al., 2004; Hocke & Schlegel, 1996; Nicolls et al., 2014). Frissell et al. (2016) found that medium-scale, daytime TIDs from the Super Dual Auroral Radar Network (SuperDARN) were strongly correlated with the strength of the polar vortex instead of geomagnetic activity. Recently, Becker, Goncharenko, et al. (2022) used the nudged HIgh Altitude Mechanistic general Circulation Model (HIAMCM) to show that wintertime, higher-order GWs in the upper mesosphere and thermosphere are much weaker during a sudden stratospheric warming than during a period when the polar vortex is strong, thereby explaining the finding of Frissell et al. (2016) in a qualitative fashion. Moreover, the characteristics of the simulated GWs in the thermosphere were found to be similar to the wave characteristics of the TIDs observed by the Global Navigation Satellite System (GNSS) in that work. Harvey et al. (2023) found a strong correlation of the observed amplitudes of wintertime TIDs with the observed GW amplitudes in the upper stratosphere. These studies illuminate the important connection between TIDs and the polar vortex.

Recently, upward and downward, northwestward and northward-propagating GWs were observed by the Arctic Lidar Observatory for Middle Atmosphere Research (ALOMAR) in northern Norway at 16.08° E, 69.38°N at $z = 45–75$ km on 12–14 January 2016 (V23). During this time, the polar vortex was the strongest and coldest as during the previous 68years (Matthias et al., 2016), which led to an unusual circulation in the mesosphere during January 2016 (Stober et al., 2017). Using model results from the nudged HIAMCM, it was found that these GWs were secondary GWs generated at ~35°E, ~60°N and $z \sim 54–60$ km from the atmosphere's response to being unbalanced by the dissipation of primary GWs from (i.e., generated/amplified by) the "core" of the polar vortex jet over Europe at 52–54°N at $z \sim 25–40$ km (V23). Here we define the core of the polar vortex jet as being the region(s) where the wind is maximum in the stratospheric jet. (In this case, the jet core was maximum at $z \sim 50$ km.) That work also found excellent agreement between the simulated primary and secondary GWs and observations by the Atmospheric InfraRed Sounder (AIRS) and the Rayleigh lidar at ALOMAR, respectively. Note that higher-order, thermospheric GWs with relatively large amplitudes are also generated when the polar vortex jet is not as strong as during this event (see Becker, Goncharenko, et al. (2022)). Thus, the cold, strong

nature of the polar vortex jet during this event is not a necessary condition to generate higher-order, thermospheric GWs.

In Vadas et al. (2024) (hereafter V24), we extended the V23 study into the mesosphere and thermosphere, and found that the vertical shear of the horizontal wind in the entrance, core and exit regions of the major and minor cores of the polar vortex jet were important for generating higher-order, medium to large-scale thermospheric GWs. Here we define the "entrance" region where the wind is constricted into a smaller area of the jet core with increasing wind speed, and the exit region where the air is expanding out of the core into a larger area with decreasing wind speed (Andrews et al., 1987; Plougonven & Zhang, 2014). In this paper, we define small, medium and large GW scales as $\lambda_H < 100$ km, $100 \leq \lambda_H < 1000$ km, and $1000 \leq \lambda_H < 4447$ km, respectively. Because the secondary GWs had large periods, they propagated at low ascent angles for large horizontal distances, thereby causing the effects of secondary and higher-order GWs from the polar vortex to be spread out over most latitudes (i.e., from low latitudes to the polar region) in the northern hemisphere mesosphere-lower-thermosphere (MLT) and thermosphere (V24).

In this paper, we model the TIDs generated by the higher-order GWs "from" (hereafter: from=generated/magnified by/via MSVC) the polar vortex during 11–15 January 2016 using the Sami3 is Also a Model of the Ionosphere (SAMI3) (Huba et al., 2000). Here we input the neutral wind from the nudged HIAMCM into the SAMI3. Because neither model contains geomagnetic forcing, all simulated GWs and TIDs are caused by lower/middle atmospheric GW sources. An important component of this study involves comparing the simulated GWs and TIDs with diverse observations to assess the accuracy of our models and deepen our understanding of the physical processes driving the generation of quiet-time thermospheric GWs and TIDs. Note that the HIAMCM and SAMI3 were successfully coupled previously to model the secondary GWs and TIDs from the Hunga Tonga-Hunga Ha'apai volcanic eruption on 15 January 2022 (Huba et al., 2023; Vadas, Becker, Figueiredo et al., 2023; Vadas, Figueiredo et al., 2023); in that case, good agreement was obtained with the neutral winds measured by the Michelson Interferometer for Global High-resolution Thermospheric Imaging (MIGHTI) on the National Aeronautics and Space Administration (NASA) Ionospheric Connection Explorer (ICON) satellite, with the TIDs from GNSS total electron content (TEC) observations, and with ionosonde data over the continental US (CONUS).

We review the HIAMCM and SAMI3 in Section 2. In Section 3, we show the simulated GWs and compare with observations. We show the simulated GWs and TIDs in Section 4. Section 5 contains results for the simulated and observed EPBs. We compare our modeled GWs and TIDs with observed TIDs in Section 6. Section 7 contains our conclusions. Appendix A shows the traveling atmospheric disturbances (TADs) observed by the GOCE and CHAMP and compares these TADs to our model results.

2. Modeling the GWs and TIDs

2.1. Modeling the GWs Using the HIAMCM

The HIAMCM is a GW-resolving, high-resolution, whole-atmosphere model for neutral dynamics (Becker & Vadas, 2020). It employs a spectral dynamical core with a terrain-following hybrid vertical coordinate, a correction for non-hydrostatic dynamics, and consistent thermodynamics in the thermosphere. This model utilizes a triangular spectral truncation at wavenumber of 256, corresponding to a horizontal grid spacing of ~52 km. Our current version has a model-top altitude of $z \sim 450$ km, has an altitude-dependent vertical resolution, includes 280 full levels, and has an effective horizontal resolution of $\lambda_H \simeq 200$ km. Resolved GWs are dissipated predominantly by macro-turbulent diffusion at $z < 200$ km using the Smagorinsky-type diffusion scheme, and by molecular diffusion at higher altitudes. Topography and a simple ocean model are fully taken into account, as well as radiative transfer, boundary layer processes, and the tropospheric moisture cycle. To simulate observed events (Becker, Vadas, et al., 2022), we nudge the large scales of the HIAMCM from the ground to $z \sim 70$ km to NASA's Modern-Era Retrospective analysis for Research and Applications, Version 2 (MERRA-2) reanalysis (Bosilovich et al., 2015). The model data used here is identical to that in V24.

2.2. Modeling the TIDs Using the SAMI3

SAMI3 is a three-dimensional, global, physics-based model of the ionosphere/plasmasphere system. It is based on the original SAMI2 model (Huba et al., 2000). SAMI3 models the plasma and chemical evolution of seven

ion species (H^+, He^+, N^+, O^+, $N_2{}^+$, NO^+, and $O_2{}^+$). The temperature equation is solved for three ion species (H^+, He^+ and O^+) and for the electrons. The SAMI3 grid spacing is 0.5° in longitude. In latitude, the spacing is 0.15° near the magnetic equator, 1° at ∼40° latitude, and 1.5° in the high-latitude region. A feature of SAMI3 used in this study is the implementation of a fourth order flux-corrected transport scheme for E × B transport perpendicular to the magnetic field. The HIAMCM provides the neutral wind and associated GW perturbations to SAMI3 to capture the dynamics of the ionosphere and TIDs (one-way coupling). However, the HIAMCM does not include the constituent components of the thermosphere (i.e., O, O_2, NO, H, He, N, and $N0_2$ densities); SAMI3 uses the empirical model NRLMSIS 2.0 (Emmert et al., 2021) to provide these needed densities here. SAMI3 then determines the ionospheric response, including the TIDs generated by the GWs. The output cadence of the SAMI3 data is 10 min here. Further details are given in Huba et al. (2023), and references therein.

3. Simulated GWs and Comparison With Observations

3.1. GWs From the Entrance, Core, and Exit Regions of the Polar Vortex Jet

Figure 1 shows T' at 0 UT on 13 January 2016 from the HIAMCM for GWs with $\lambda_H < 2001$ km. Here, T' is computed from the wavenumber decomposition in terms of spherical harmonics, where T' includes only total horizontal wavenumbers from 20 to 256, corresponding to horizontal wavelengths smaller than 2,001 km (Becker, Vadas, et al., 2022). Vectors show $(\overline{U}, \overline{V})$. Here, the background zonal and meridional wind, $\overline{U}$ and $\overline{V}$, contain all waves from the HIAMCM with total horizontal wavenumber <9 (with respect to spherical harmonics decomposition), which corresponds to $\lambda_H > 4447$ km. Figure 1a shows the results at $z = 40$ km. Green contours outline the total background wind, $\sqrt{\overline{U}^2 + \overline{V}^2}$, at $z = 50$ km, which is the height where the wind in the polar vortex jet is maximum (V23). Primary GWs are located over (a) the core of the polar vortex over Europe with phase lines approximately parallel to the wind (green arrows), (b) the entrance regions of the polar vortex jet with phase lines approximately perpendicular to the wind (turquoise arrows) and (c) the exit region of the polar vortex jet with phase lines approximately perpendicular to the wind (purple arrow). Figure 1b shows the GWs at $z = 70$ km. The GWs over Europe with phase lines approximately parallel to the wind are nearly entirely absent here. According to V24, the GWs at $z = 70$ km contain both primary and secondary GWs. Figure 1c shows the GWs at $z = 100$ km in the MLT. At this altitude, the morphology of the GWs are quite different from those GWs at $z = 40$ and 70 km. In particular, the GWs over Europe have arc-like structures with an apparent northeastward propagation direction, and the GWs over Asia are more coherent with larger λ_H. Figure 1d shows the GWs at $z = 120$ km. Partial concentric arcs and rings are seen over the Atlantic Ocean and Europe. Figure 1e shows the GWs at $z = 250$ km. Partial concentric arcs and rings are seen over Europe and Asia. According to V24, these are higher-order GWs. Note that in general, the thermospheric GWs tend to propagate against the background wind.

We now compare the HIAMCM GWs with those observed by the Atmospheric InfraRed Sounder (AIRS) (Hoffmann et al., 2013). The first column of Figure 2 shows daily-averaged temperature variances, $(T')^2$, at $z = 40$ km from the HIAMCM on 11–14 January for GWs with $\lambda_H < 2001$ km. The core of the polar vortex jet, illuminated here for $U_H = \sqrt{\overline{U}^2 + \overline{V}^2} = 100$ m/s at $z = 50$ km (blue contours), is located over Europe and the northern Atlantic Ocean. This jet is fairly consistent day-to-day in amplitude and location. The vortex edge (yellow lines, computed using the method from Harvey et al. (2002)) roughly follows the poleward flank of the wind maximum. The GWs tend to be concentrated at the outer edge of the jet near the vortex edge, as discussed in V23.

We now (a) remove those simulated GWs with $\lambda_H > 1000$ km by performing a running mean smoothing of 1,000 km in width on the HIAMCM T' then subtracting this map from T', then (b) weight the resulting T' vertically with the following AIRS weighting function:

$$\tilde{T} = \frac{\int T' \chi dz}{\int \chi dz}, \tag{1}$$

where

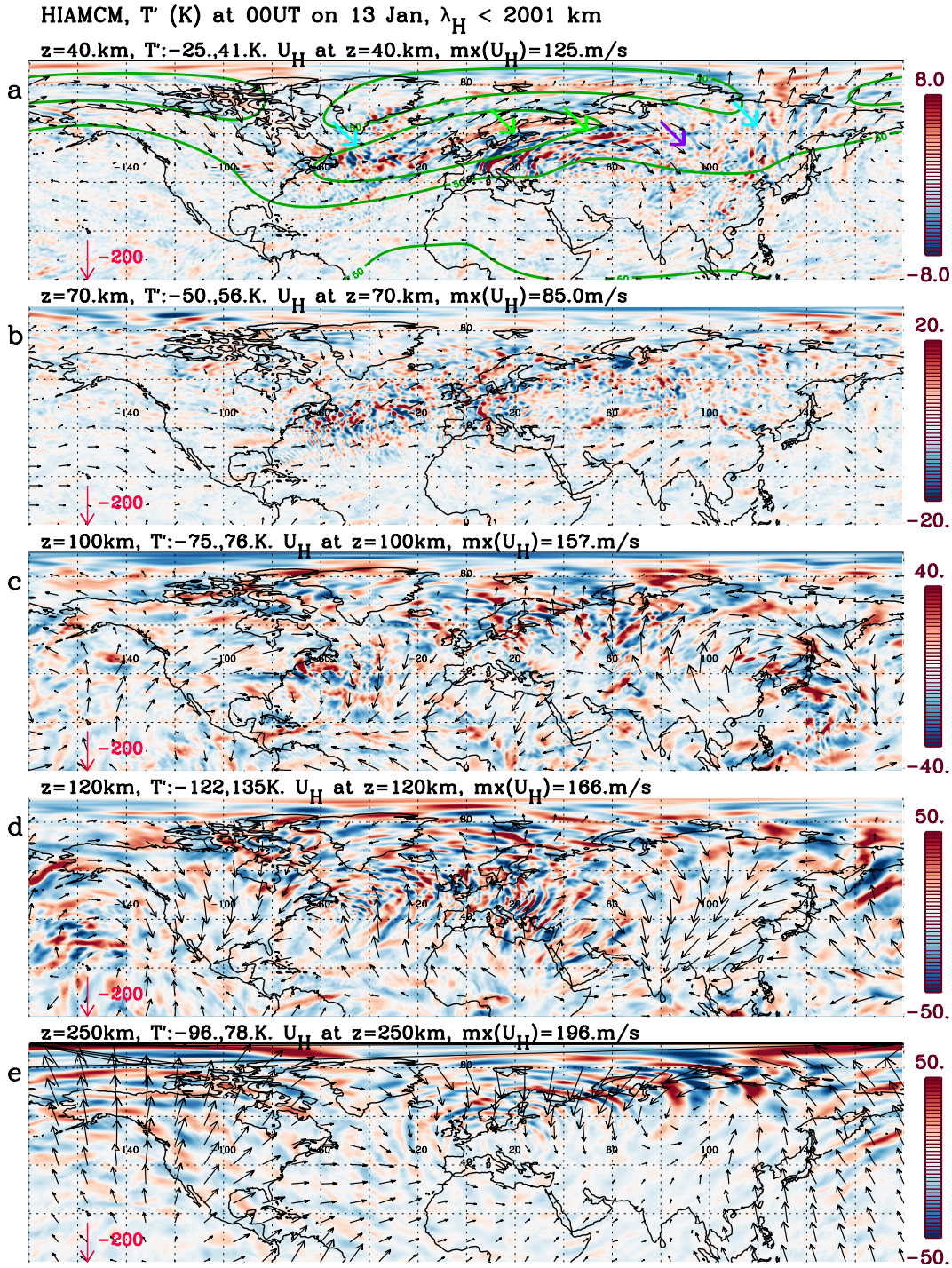

Figure 1. T' (colors, in K) at 0 UT on 13 January 2016 from the HIAMCM for GWs with $\lambda_H < 2001$ km. (a): $z = 40$ km. (b): $z = 70$ km. (c): $z = 100$ km. (d): $z = 120$ km. (e): $z = 250$ km. The horizontal background wind $(\overline{U}, \overline{V})$ are shown at each altitude as vectors. The downward red arrows in the lower left-hand corners show $\overline{V} = -200$ m/s. Green contours in (a) show $\overline{U}_H = \sqrt{\overline{U}^2 + \overline{V}^2} = 50$, 100, and 150m/s at $z = 50$ km, and arrows show GWs over the entrance (turquoise), core (green) and exit (purple) regions of the polar vortex jet. Minimum and maximum values of T' and $\overline{U}_H$ are given in each caption. The colors are oversaturated to see the GWs.

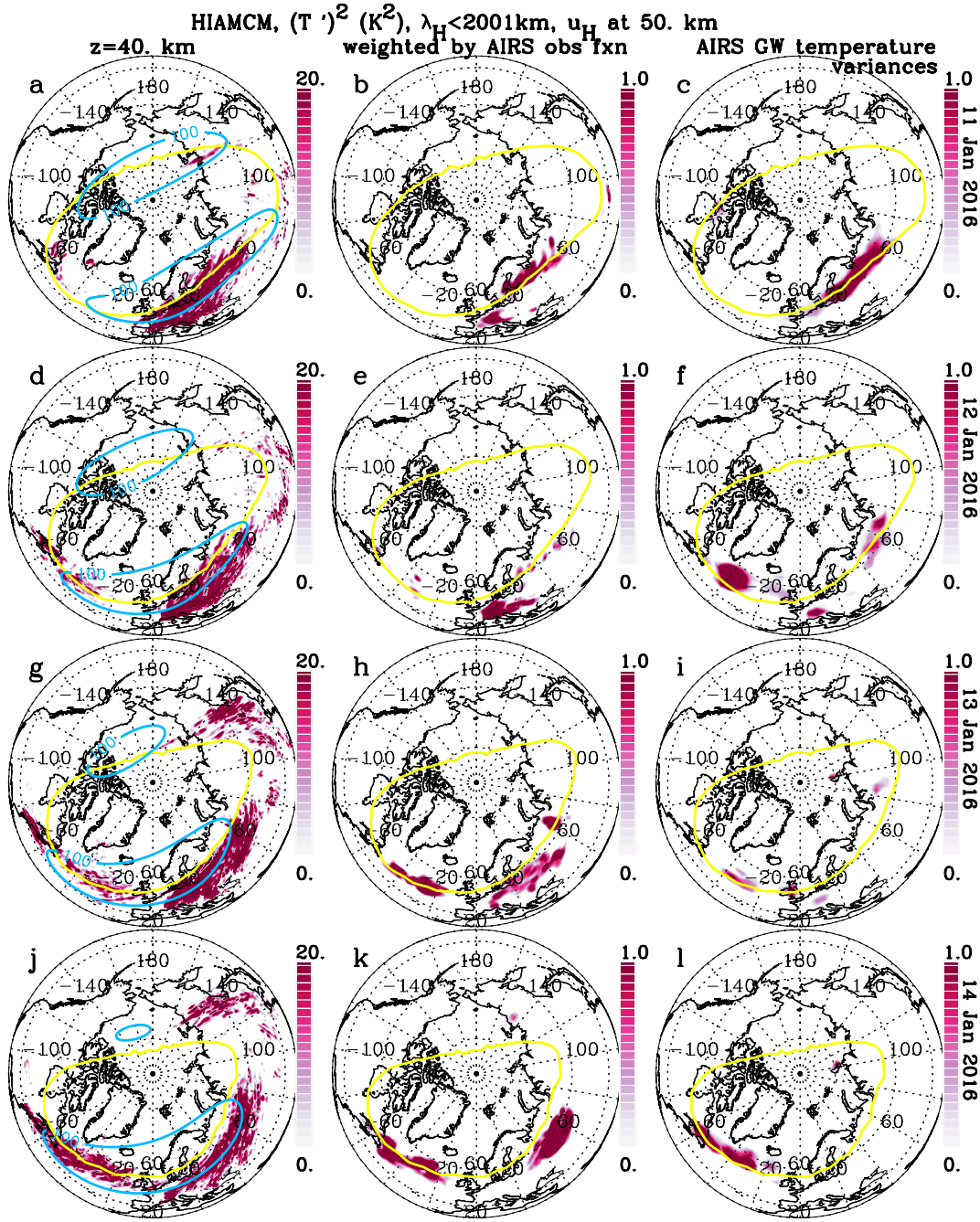

Figure 2. Left column: $(T')^2$ (colors, in K^2) at $z = 40$ km averaged daily on 11, 12, 13, and 14 January 2016 (in a, d, g, j, respectively) from the HIAMCM for GWs with $\lambda_H < 2001$ km. The background wind speed, $U_H = \sqrt{\overline{U}^2 + \overline{V}^2}$, of 100 m/s is shown at $z = 50$ km (blue contours). Middle column: Same as first column, except showing the observationally-weighted temperature $(\tilde{T})^2$ from Equations 1 and 2 (see Figure 3). Right column: $(T')^2$ observed by AIRS and averaged daily on 11, 12, 13, and 14 January 2016 (in c, f, i, l, respectively). The yellow lines show the vortex edge.

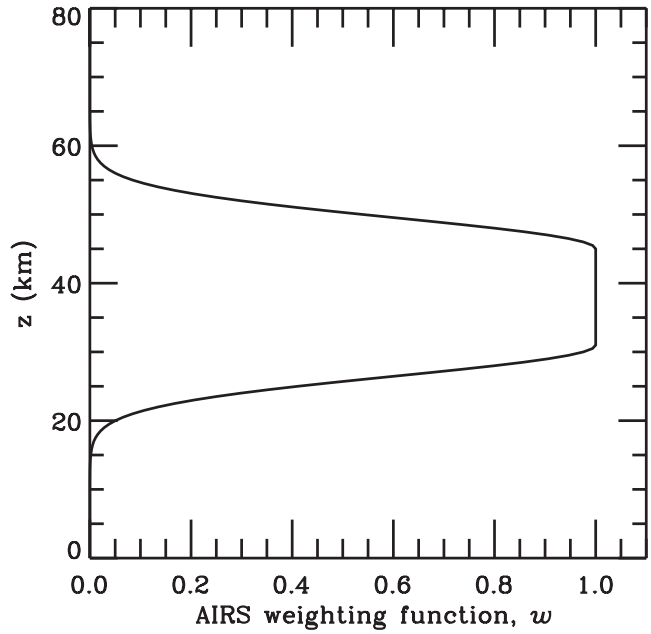

Figure 3. The AIRS temperature weighting function, χ, given by Equation 2 with $\sigma_z = 4.5$ km, $z_{\text{mid}} = 38$ km, and $\Delta = 7$ km.

$$\chi(z) = \begin{cases} \exp\left(-0.5\left([z-(z_{\text{mid}}-\Delta)]/\sigma_z\right)^2\right) & \text{for } z \le z_{\text{mid}}-\Delta \\ 1 & \text{for } z_{\text{mid}}-\Delta \le z \le z_{\text{mid}}+\Delta \\ \exp\left(-0.5\left([z-(z_{\text{mid}}+\Delta)]/\sigma_z\right)^2\right) & \text{for } z \ge z_{\text{mid}}+\Delta. \end{cases} \quad (2)$$

We choose $\sigma_z = 4.5$ km, $z_{\text{mid}} = 38$ km and $\Delta = 7$ km so that χ is similar to Fig. 4a from Hoffmann et al. (2014). This observational filter removes GWs with $|\lambda_z| < 16-24$ km. χ is shown in Figure 3. Note that χ is similar to the AIRS vertical weighting function used by Becker, Vadas, et al. (2022). The second column of Figure 2 shows the daily-averaged observationally-filtered HIAMCM temperature, $\left(\tilde{T}\right)^2$, from Equation 1. Most of the GWs are eliminated via this observational filter, although GWs remain over eastern Canada, the Atlantic Ocean, and western Asia. The third column of Figure 2 shows the temperature variances observed by AIRS. GWs are seen over the Atlantic Ocean on 12–14 January, and over Europe and western Asia on 11–13 January. Good agreement between the observed and simulated GWs is seen on 11, 13–14 January over the Atlantic Ocean and eastern Canada, and on 11–12 January over Europe and western Asia. On 13–14 January however, the GWs observed by AIRS have weak amplitudes over Europe, while the observationally-filtered HIAMCM GWs have large amplitudes over Europe. It is likely not a coincidence that the polar vortex event over Europe ramps up near the end of 12 January and continues through the end of 14 January (V23). A possible explanation for the poor agreement over Europe during 13–14 January in Figures 2h–2i and 2k–2l is that the MERRA-2 (eastward) wind speed of the polar vortex jet is larger than the actual wind speed over Europe on 13–14 January. The measured winds incorporated into the MERRA-2 reanalysis product contain balloon measurements at $z < 26$ km; at higher altitudes, the MERRA-2 reanalysis generates winds using physics that does not include MSVC of GWs from the polar vortex jet, and therefore does not include the change of the background wind from the dissipation of these GWs. Near the end of 12 January, the large-amplitude, westward-propagating, primary GWs generated by the polar vortex jet would partially decelerate the eastward wind of the polar vortex jet over Europe where they dissipate at $z \sim 50-70$ km. Such deceleration would reduce the wind speed of the polar vortex jet, thereby causing $|\lambda_z|$ to be smaller for the primary westward GWs during 13–14 January than on 11 January. Because the HIAMCM nudges in the large-scale MERRA-2 wind "as-is," the effect of a partially-decelerated polar vortex jet from GW dissipation would not be taken into account in the simulated GWs, thereby causing the simulated $|\lambda_z|$ to be too large over Europe during 13–14 January.

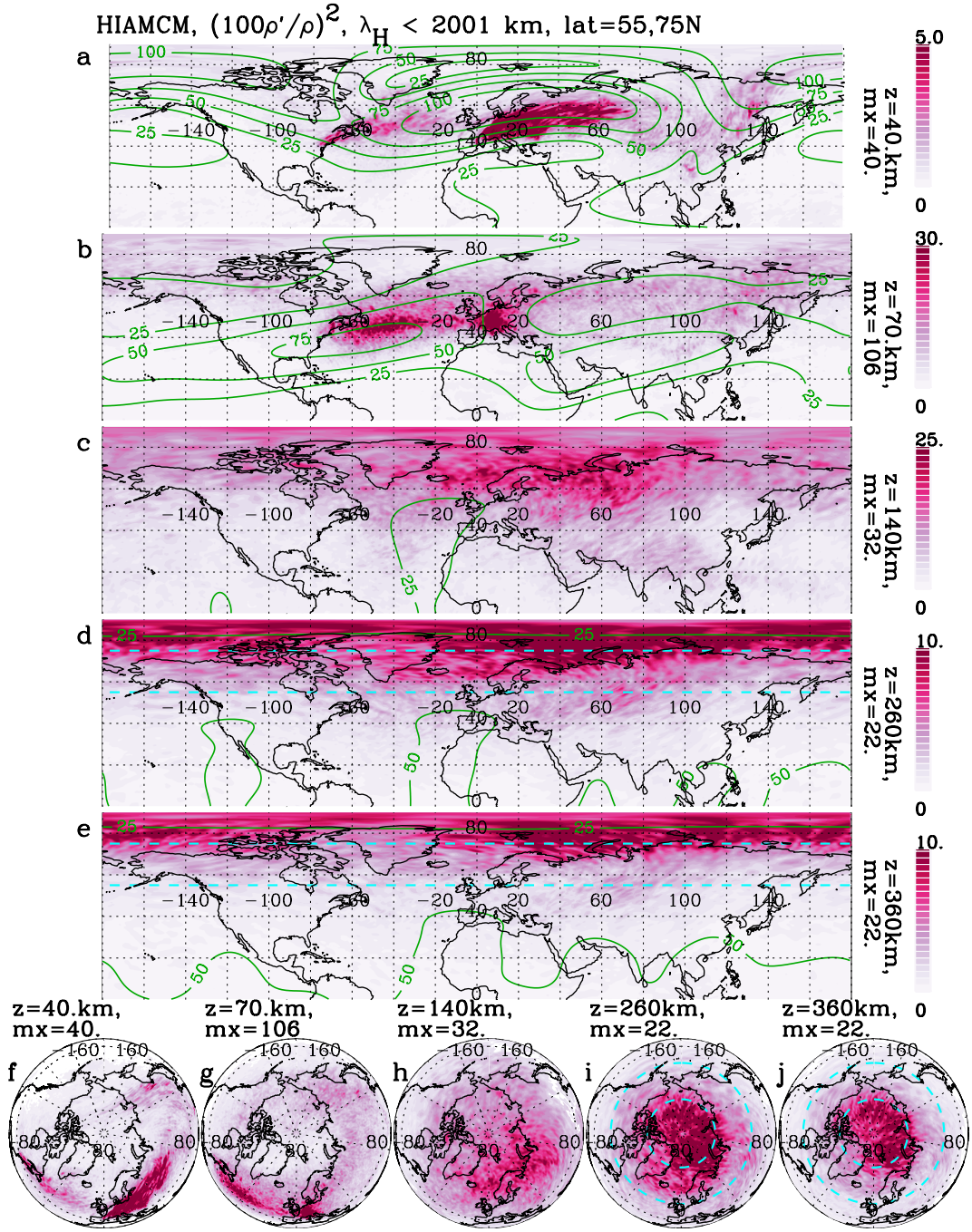

Figure 4. $(100\rho'/\overline{\rho})^2$ from the HIAMCM for GWs with $\lambda_H < 2001$ km (colors) averaged from 0 UT on 11 January to 24 UT on 14 January 2016. (a)–(e) $z = 40$, 70, 140, 260, and 360 km, respectively. Note the different color bars. (f)–(j): Polar plots at $z = 40$, 70, 140, 260, and 360 km using the same color bars as (a)–(e), respectively. Green lines in (a)–(e) show the average of $U_H = \sqrt{\overline{U}^2 + \overline{V}^2}$ during this time at each given altitude for 25, 50, 75, and 100m/s. The dash turquoise lines in (d, e, i, j) show geographic latitudes 55°N and 75°N. The colors are oversaturated to see the GWs.

3.2. Latitudinal and Altitudinal Dependencies of the Simulated GWs

Figure 4 shows the density perturbations of the GWs with $\lambda_H < 2001$ km, $(100\rho'/\overline{\rho})^2$, averaged during 11–14 January from the HIAMCM. Figures 4a and 4f show the result at $z = 40$ km. GWs occur over Europe over the major core of the polar vortex jet with amplitudes of $|\rho'/\overline{\rho}| \sim 6\%$. GWs also occur over northeastern US and Canada (including the Appalachian Mountains) over the entrance region of the major core of the polar vortex jet with amplitudes of ∼3%. Finally, GWs occur over the Asian continent over the exit region of the major core/entrance region of the minor core of the polar vortex jet with amplitudes of ∼2%. At $z = 70$ km, GWs occur at similar locations (see Figures 4b and 4g). These results are consistent with SABER observations in January whereby the observed GWs at $z = 30-70$ km occur over Europe, northern Asia, and eastern US/Canada (Fig. 4 of Trinh et al., 2018).

At $z = 140$ km, the GW distribution is spread out longitudinally and has shifted to higher latitudes (Figures 4c and 4h). Over North America, the GWs are concentrated north of 60°N. Therefore, care must be taken to identify the sources of southward-propagating thermospheric GWs seen at this height (England et al., 2021), since they could be higher-order GWs from below rather than from geomagnetic forcing. At $z = 260$ and 360 km, the GWs are concentrated poleward of 55°N and are spread out uniformly in longitude, with the largest-amplitude GWs occurring poleward of 75°N with $|\rho'/\overline{\rho}| \sim 4-5\%$ (see Figures 4d–4e and 4i–4j). A similar high-latitude GW distribution was seen in a previous model study at $z = 300$ km, although additional enhancements occurred over North America/Greenland and Europe (Fig. 13j–l of Becker & Vadas, 2020). The amplitudes and latitudinal distribution of the GWs in Figure 4 agree with quiet-time satellite measurements of TADs from the DE2 satellite for which $|\rho'/\overline{\rho}| \sim 5\%$ (Fig. 7 of Hedin & Mayr, 1987), from the CHAMP satellite for which $|\rho'/\overline{\rho}| \sim 6-7\%$ poleward of 60°N (Fig. 3 of Bruinsma & Forbes, 2008), from the GOCE satellite for which $|\rho'/\overline{\rho}| \sim$ few% (Liu et al., 2017), and from GOCE/CHAMP satellites for which $|\rho'/\overline{\rho}| \sim 1-2\%$ (Figs. 4,6 of Trinh et al., 2018) and $|\rho'/\overline{\rho}| \sim 2-4\%$ (Figs. 3–6 of Xu et al., 2021). Our results are also consistent with Park et al. (2014), who analyzed TADs with Kp < 4.

The high-latitude, winter thermospheric GW hotspot in the northern polar region shown in Figures 4i and 4j is quite remarkable, given that (a) the primary GW hotspots are located at midlatitudes (see Figure 4a), and (b) none of the simulated GWs are generated by geomagnetic forcing. Therefore, higher-order GWs generated/magnified by the polar vortex jet likely contribute significantly to the variability of the mid to high latitude winter thermosphere and, correspondingly, to the ionosphere. Such wintertime GWs due to MSVC of GWs "from below" (i.e., primary GWs originating at $z \ll 120$ km) could easily be mistaken as being generated by geomagnetic forcing because they appear to originate from high latitudes and propagate southward during the daytime (V24).

To gain additional insight, we show the quiet-time TADs observed by GOCE in 2009–2013 and by CHAMP in 2004–2007 in Appendix A. Although these data do not overlap with our study period, there are many similarities with our simulated GWs. In particular, a significant portion of the observed TADs have a uniform distribution in longitude; these "longitudinally-uniform" TADs are located at high latitudes and have similar amplitudes as the simulated GWs in Figure 4. Thus it is possible that the longitudinally-uniform TADs observed by GOCE and CHAMP may have been due to higher-order GWs from below.

4. GWs and TIDs Simulated by HIAMCM-SAMI3

The left column of Figure 5 shows $100\ T'/\overline{T}$ from the HIAMCM at $z = 220$ km for various times from 11 to 14 January for GWs with $\lambda_H < 2001$ km. The polar vortex jet is located over Europe and the northern Atlantic Ocean (blue contours). Arrows show the approximate location of the entrance (turquoise), core (green) and exit (purple) regions of the polar vortex jet. Southeastward-propagating, higher-order GWs are seen at 8–9 UT (∼8–15 local time (LT)) over Europe, northern Africa and eastern Asia during all four days (green arrows in Figures 5a, 5c, 5g, and 5i). These GWs propagate approximately antiwindward since the background tidal wind is northwest and northward on the dayside (Becker, Goncharenko, et al., 2022). These GWs are higher-order GWs from MSVC of the primary GWs generated/amplified by the major core of the polar vortex jet (V24). Simultaneously, east, northeast and northward-propagating concentric and arc-like GWs are seen over northeastern Canada, Greenland and the Atlantic Ocean (radiating away from the turquoise arrows in the Atlantic sector) at ∼2–8 LT during all 4 days because the background thermospheric wind is south, southwest and westward at those LTs (Becker, Goncharenko, et al., 2022). These GWs are generated from MSVC of primary GWs generated/amplified by the

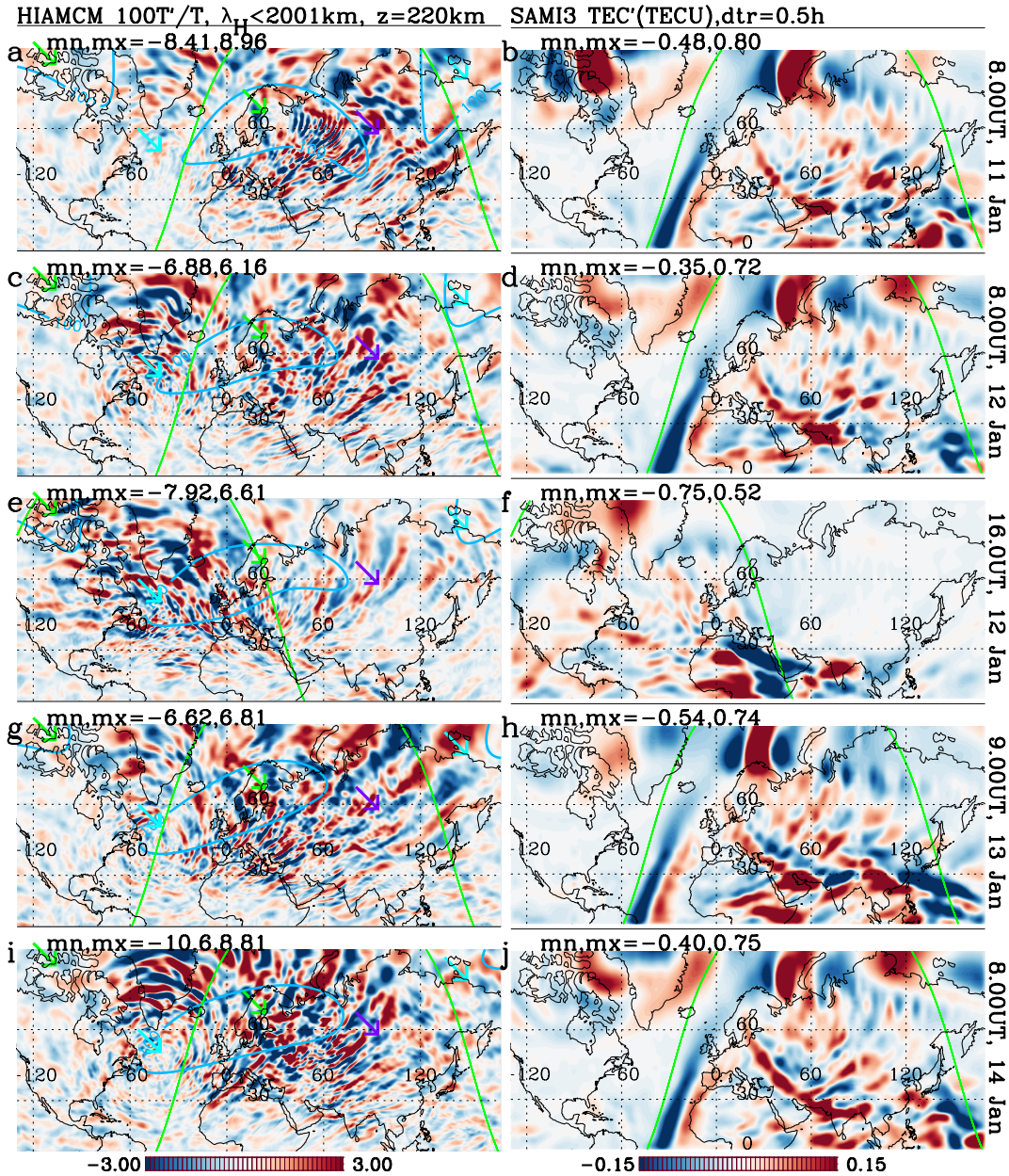

Figure 5. (a): 100 $T'/\overline{T}$ (colors) from the HIAMCM at $z = 220$ km at 8 UT on 11 January 2016 for GWs with $\lambda_H < 2001$ km. The background wind speed of $U_H = 100$ m/s is shown at $z = 50$ km (blue contours). The arrows show the approximate location of the entrance (turquoise), core (green) and exit (purple) regions of the polar vortex jet. (b) dTEC (in TECU) from the SAMI3 using a 30-min detrend window at 8 UT on 11 January 2016. Rows 2–5: Same as row 1 but at 8 UT on 12 January, 16 UT on 12 January, 9 UT on 13 January, and 8 UT on 14 January, respectively. Green lines show the sunrise and sunset solar terminators. Minimum and maximum values are given at the top of each panel. The colors are oversaturated to see the GWs.

entrance of the major core of the polar vortex jet (V24). The right column of Figure 5 shows the TEC perturbations, dTEC, from the SAMI3 using a 30-min detrend window at the same times as the left column. Concentric and arc-like TIDs generated by the higher-order GWs from the entrance, core and exit regions of the polar vortex jet are seen during the daytime. These TIDs occur over Europe/North Africa/Asia at 8–9 UT (see Figures 5b, 5d, 5h, and 5j), and over North/Central America and the Atlantic Ocean at 16 UT (see Figure 5f). As was seen for the TIDs generated by GWs from the Tonga volcanic eruption, SAMI3 is not able to resolve medium-scale TIDs (MSTIDs) with $\lambda_H < 600$ km (Vadas, Figueiredo et al., 2023). In addition, it is important to note that the SAMI3 TIDs are not accurate at high latitudes (>60°) due to the sparsity of flux tubes and resulting low horizontal

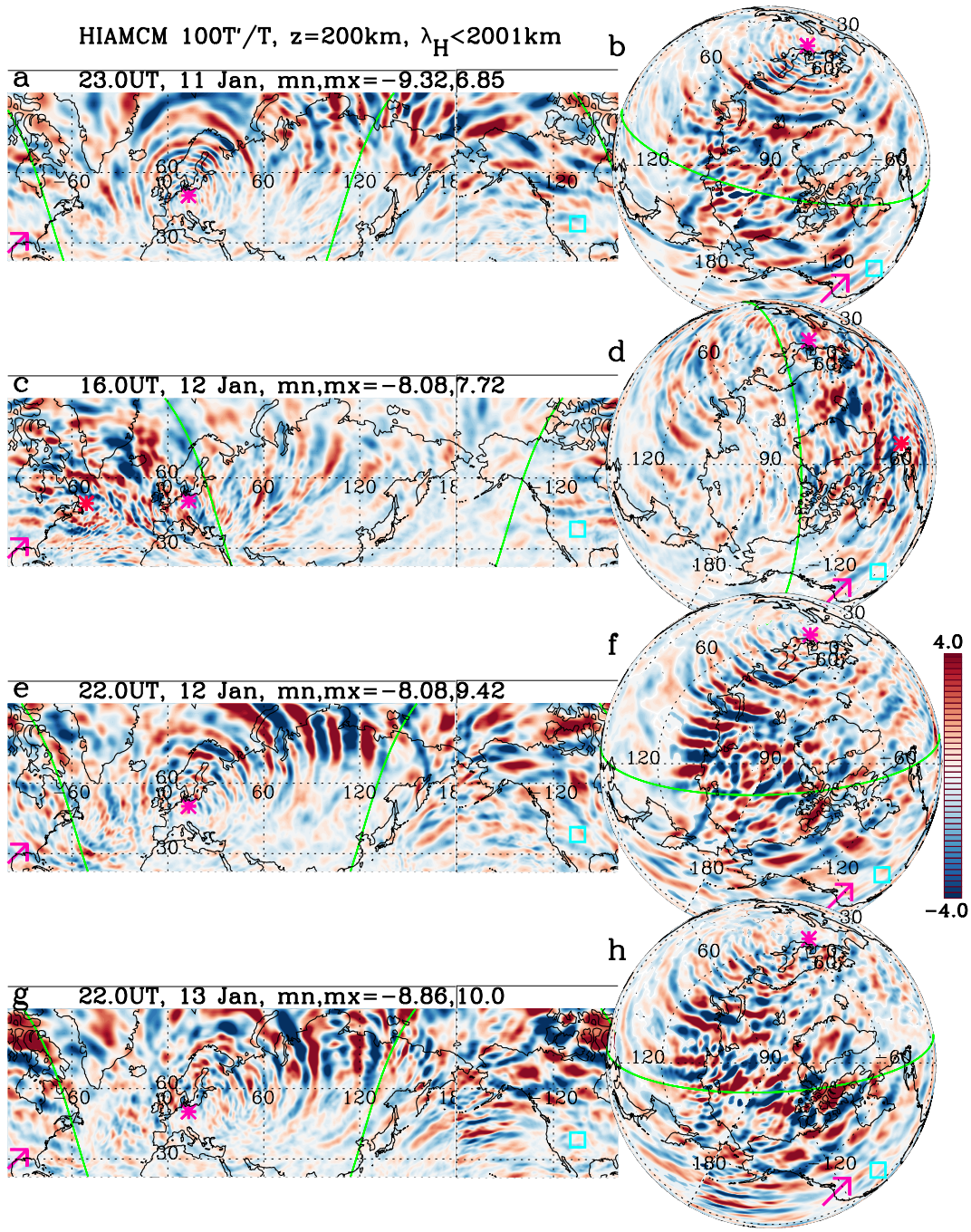

Figure 6. Horizontal slices of $100T'/\overline{T}$ (colors) from the HIAMCM at $z = 200$ km for GWs with $\lambda_H < 2001$ km at (a–b) 23 UT on 11 January 2016, (c–d) 16 UT on 12 January, (e–f) 22 UT on 12 January, and (g–h) 22 UT on 13 January. The pink asterisks are located at (13°E, 52°N). The red asterisks in panels (c) and (d) are located at (51°W, 51°N). The turquoise squares are located at Boulder, Colorado (100°W, 40°N). Pink arrows show the GWs over the CONUS. Green solid lines show the sunrise and sunset solar terminators. The colors are oversaturated to emphasize the waves.

resolution there. The sunrise terminator wave is clearly visible here (e.g., in Figures 5b, 5d, 5h, and 5j over the eastern Atlantic Ocean) (Gasque et al., 2024, and references therein). These waves are not visible in the left column of Figure 5 because they have $\lambda_H \sim 3000$ km (Forbes et al., 2008).

At 16 UT on 12 January in Figure 5e, concentric and arc-like GWs occur over the entrance, core and exit regions of the major polar vortex jet (turquoise, green and purple arrows, respectively). Simultaneously, daytime GWs

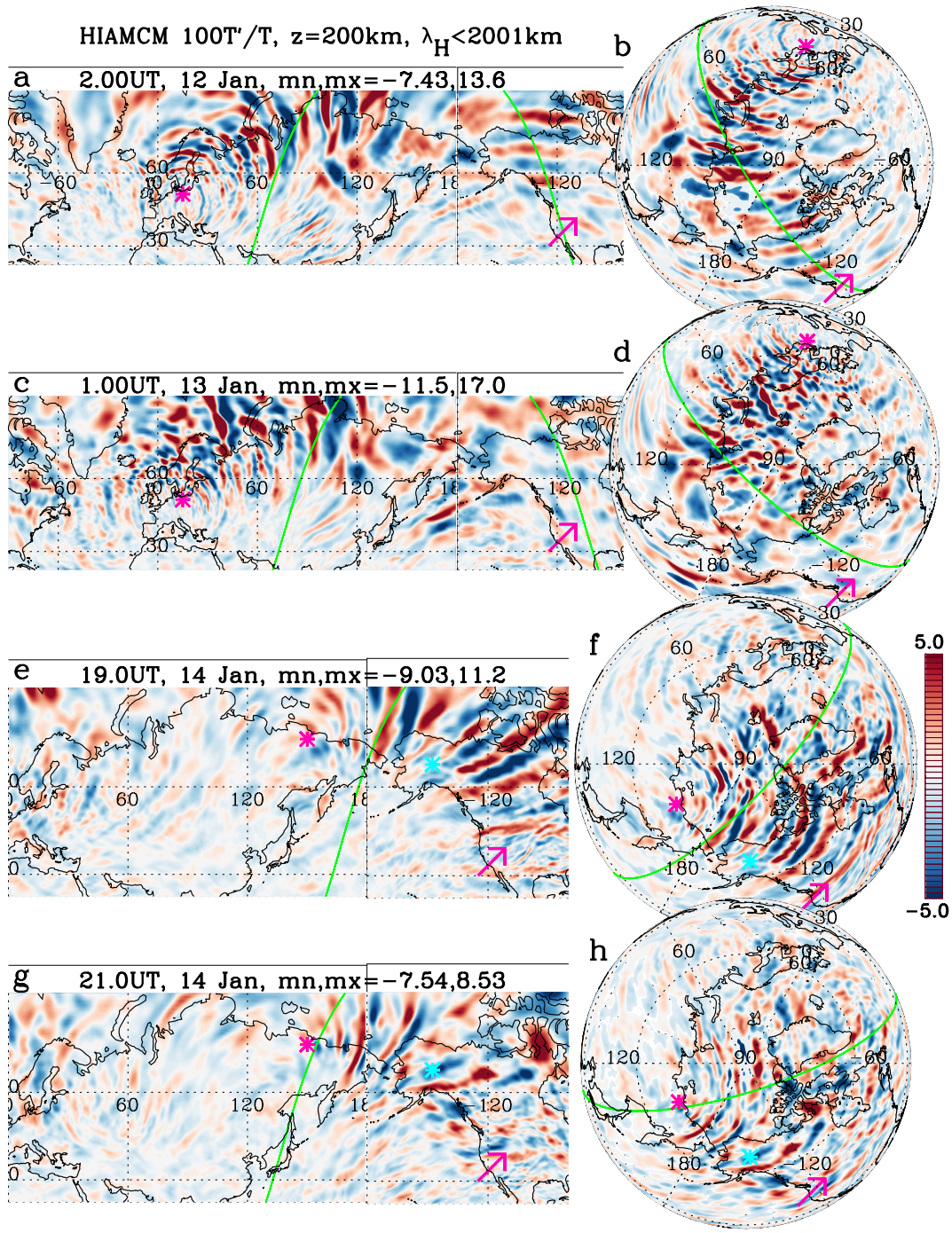

Figure 7. Horizontal slices of $100T'/\overline{T}$ from the HIAMCM at $z = 200$ km for GWs with $\lambda_H < 2001$ km at (a–b) 2 UT on 12 January 2016, (c–d) 1 UT on 13 January, (e–f) 19 UT on 14 January, and (g–h) 21 UT on 14 January. The pink asterisks are located at (15°E, 53°N) (a–d) and at (150°E, 70°N) (e–h). The turquoise asterisks show PFISR (147.47°W, 65.13°N) (e–h). Pink arrows show the GWs over the CONUS. Green solid lines show the sunrise and sunset solar terminators. The colors are oversaturated to emphasize the waves.

propagate southward over North America at ∼9–12 LT. Since geomagnetic activity is not included in this model run, what is the source of the GWs over North America? Figure 6 shows horizontal slices and global perspectives of $100T'/\overline{T}$ at $z = 200$ km for GWs with $\lambda_H < 2001$ km in the northern hemisphere during 11–13 January. (The second row is the same time as in Figure 5e.) Several wave sources are seen. The main source is located over Europe, as indicated by the pink asterisks at (13°E, 52°N). These are the higher-order GWs generated/amplified

by the major core of the polar vortex jet (V24). (Note that the primary GWs for this source are mainly GWs generated by the vertical shear of the horizontal wind in the stratospheric polar vortex jet, but also include MWs generated over the Alps and Carpathian Mountains.) Another source is located over the entrance region of the major core of the polar vortex jet (V24), as indicated by the red asterisks in Figures 6c and 6d at (51°W,51°N). These different GW packets create constructive/destructive interference patterns where they intersect. Many of the GWs that propagate southward across North America (pink arrows) originate over northern Europe (see pink asterisks at 13°E, 52°N), and cross over the northern polar region (including Greenland and/or the northern Atlantic Ocean) to North America (e.g., Figures 6b, 6f, and 6h). For example, the GWs generated over Europe propagate over Greenland then southward over Boulder, Colorado (100°W,40°N) on 11 January (turquoise squares in Figures 6a and 6b).

Figures 7a and 7b shows a horizontal slice and global view of $100T'/\overline{T}$ for GWs with $\lambda_H < 2001$ km from the HIAMCM at $z = 200$ km at 2 UT on 12 January. GWs propagate southwestward across the CONUS (pink arrows). Most of these GWs are higher-order GWs generated/amplified by the major core of the polar vortex jet over northern Europe (V24). These concentric GWs originate over Europe near (15°E, 53°N) (pink asterisks), then propagate over the Arctic region then southward over Canada and the CONUS (see Figure 7b). The same situation repeats itself 23 hr later (1 UT on 13 January in Figures 7c and 7d), whereby higher-order, concentric GWs are again generated/amplified by the major core of the polar vortex jet over northern Europe (pink asterisks), then propagate over the polar region then southwestward over the CONUS (pink arrows). On this day, however, there is significant constructive/destructive interference of these GWs with GWs from other sources. In particular, GWs are generated over the northern Asian continent then also propagate over the polar region then southward over the CONUS (see Figure 7d).

We now show that higher-order GWs from the polar vortex jet propagate southeastward over Alaska on 14 January. As we show in Section 6.2, daytime TIDs are observed simultaneously by the Poker Flat Incoherent Scatter Radar (PFISR). Figures 7e and 7f shows a horizontal slice and global view at 19 UT on 14 January (11 LT at Fairbanks, Alaska). Daytime GWs propagate southeastward over Alaska and approximately southward across the CONUS (pink arrows). (The turquoise asterisks show PFISR at (147.47°W, 65.13°N)). These GWs are generated over the northern Asian continent near the exit region of the major core and entrance region of the minor core of the polar vortex jet (pink asterisks at (150°E, 70°N)). At this time, the background wind from the diurnal tide in the thermosphere is approximately northward over North America, which allows for the southward propagation of GWs over Alaska and the CONUS. Figures 7g and 7h show the corresponding results 2 hr later. Again, GWs are generated over the northern Asian continent (pink asterisks), propagate southeastward across Alaska, then southward over the CONUS (pink arrows).

Finally, we note from Figure 6 (rows 1, 3–4) and Figure 7 (row 4) that GWs generated over Europe/Asia propagate over the polar region from the nightside to the dayside (southward over North America) at ∼21–23 UT for four consecutive days in a row. This occurs because the thermospheric wind is southward over Europe at LT midnight and is northward over North America at LT noon (Becker, Goncharenko, et al., 2022). Figures 6 and 7 show that cross-polar GW propagation occurs over a large range of times, ∼16–26 UT (see Movie S7 from V24), and is thus likely a common wintertime occurrence in the northern hemisphere.

Because of SAMI's low horizontal resolution at >60°N, we do not show the simulated TIDs here corresponding to Figures 6 and 7. However, because TIDs are generated by GWs through ion-neutral collisions and are not self-sustaining, we expect cross-polar GWs to generate cross-polar TIDs. Indeed, we show in Section 6.2 that the TIDs observed by PFISR agree well with the simulated GWs, thereby confirming this expectation.

We now show the day-to-day variability of the morphology, propagation directions and horizontal scales of the thermospheric GWs and TIDs during this study period. The left column of Figure 8 shows 100 $T'/\overline{T}$ from the HIAMCM over Europe, Asia and northern Africa at $z = 220$ km at 12 UT on 11–14 January for GWs with $\lambda_H < 2001$ km. Concentric and arc-like GWs propagate away from different locations, with generally larger amplitudes on 13–14 January. Note that there is significant day-to-day variability of the morphology of the GW structures. In addition, the GWs tend to have $\lambda_H \sim$ hundreds of km near their (source) centers and $\lambda_H \sim$ 500–2000 km further from their centers. This occurs because $\lambda_H \propto \mathcal{R}^2$ for GWs generated by a point source, where $\mathcal{R}$ is the horizontal radius from the GW to the center (Eq. (8) of Vadas & Azeem, 2021). The middle column of Figure 8 shows the same results for GWs with $2001 < \lambda_H < 4447$ km. Large-scale GWs with $\lambda_H \sim 3{,}000$ km are

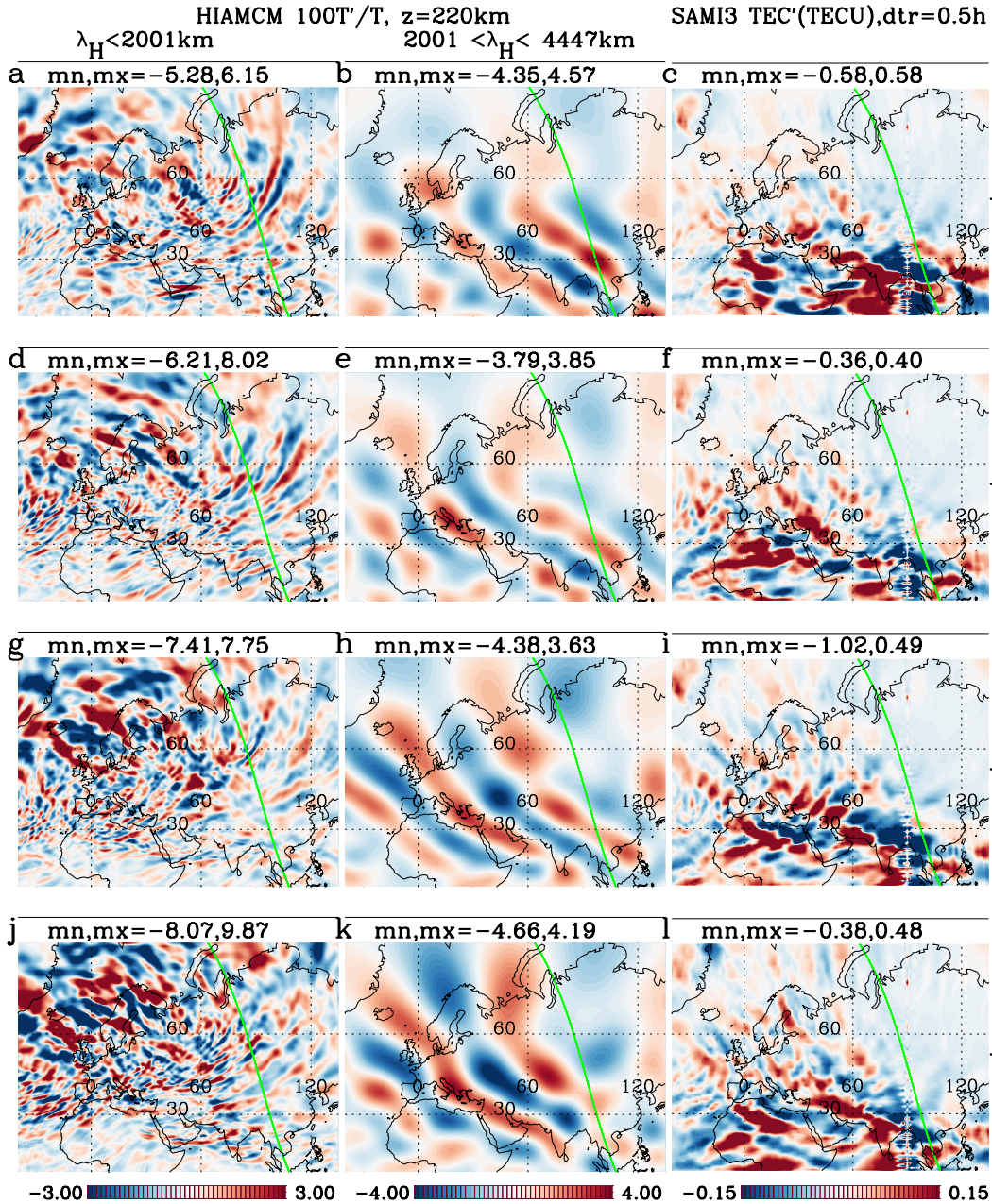

Figure 8. (a): 100 $T'/\overline{T}$ (colors) from the HIAMCM at $z = 220$ km at 12 UT on 11 January 2016 for GWs with $\lambda_H < 2001$ km over Europe, Asia and northern Africa. (b) Same as (a) but for GWs with $2001 < \lambda_H < 4447$ km. (c) dTEC (colors, in TECU) from the SAMI3 using a 30-min detrend window at 12 UT on 11 January 2016. Rows 2–4: Same as row 1 but at 12 UT on 12–14 January, respectively. Green solid lines show the sunrise and sunset solar terminators. Minimum and maximum values are given at the top of each panel. The colors are oversaturated to see the GWs.

seen having larger amplitudes on 13–14 January. These GWs mainly propagate southwestward in the antiwindward phase of the diurnal tide at ∼8–16 LT, with an estimated horizontal phase speed of $c_H \sim 650$ m/s (V24). Because of this, the medium and large-scale GWs often propagate in different directions. Note that the sum of the left and middle columns equals the full GW solution simulated by the HIAMCM. The right column of Figure 8 shows the dTEC from the SAMI3 at the same times using a 30-min detrend window. Concentric and arc-like MSTIDs and southwestward-propagating large-scale TIDs (LSTIDs) are seen which closely track the GWs in the left and middle columns, respectively. Note that the MSTIDs and LSTIDs often propagate in different directions. This is because

the MSTIDs over Europe are generated by the medium-scale concentric and arc-like GWs that propagate eastward, southeastward and southward at 12 UT due to "dissipative" filtering of the north, northwest and westward-propagating GWs from the diurnal tide (which is northwestward at this time), while the LSTIDs are generated by the large-scale GWs which mainly propagate southwestward in the northern middle thermosphere due to dissipative filtering from the background wind component of the diurnal tide at $z > 180$ km (see V24). Note that V24 showed that these large-scale, southwestward-propagating GWs were likely generated by high-latitude, large-scale LBFs generated by the dissipation of secondary GWs (from the polar vortex jet) in the MLT. Here, dissipative filtering refers to the process by which thermospheric GWs that propagate with the wind have decreased $|\lambda_z|$, which causes them to dissipate at lower altitudes from molecular viscosity (Vadas, 2007), even if they do not reach critical levels.

5. Simulated and Observed Equatorial Plasma Bubbles

Movie S1 shows the dTEC from the SAMI3 using a 30-min detrend window during 11–14 January. Concentric and arc-like TIDs over the entrance region of the polar vortex jet (over the Atlantic Ocean) contribute daily to the TID activity at ~11–18 UT, although with significant day-to-day variability. In addition, southward-propagating MSTIDs are seen over North and South America at ~15–24 UT during the daytime; these are the cross-polar higher-order GWs from the polar vortex jet over Europe and Asia (see Figures 6 and 7). Such TIDs could be misidentified as being generated by geomagnetic activity because they arise from high latitudes.

In addition, Movie S1 shows that some of the LSTIDs generated by the higher-order GWs created over Europe propagate from the northern to southern hemisphere down to ~30°S. Four snapshots at various times from 12 to 14 January are shown in Figure 9. Figures 9a and 9d shows the TIDs over the African/Indian Ocean/Australian sector while Figures 9b and 9c shows the TIDs over the South American/Pacific Ocean sector (pink arrows). In addition, note that EPBs form east of Brazil after sunset in Figures 9b and 9c (turquoise arrows). Movie S1 shows that EPBs occur daily over/east of Africa starting at ~16–17 UT and over/east of Brazil at ~22 UT each day. It is notable that the medium to large-scale TIDs/GWs from the major core of the polar vortex jet are located at the northern boundary of the EPBs over/east of Africa (e.g., at 19:00 UT on 11 January and at 16:00 UT on 12–14 January), thereby possibly aiding the formation of the EPBs (Tsunoda, 2005, 2010). A similar phenomenon is seen for the TIDs/GWs over/east of Brazil.

Figures 10a–10d shows snapshots of the dTEC from the SAMI3 using a 30-min detrend window on 13 January. The first row shows EPB occurrences at 16:30 and 18:10 UT east/over Africa, and the second row shows EPB occurrences 4–6 hr later at 22:20 and 23:00 UT east/over Brazil/South America, as indicated by the turquoise arrows. Pink arrows indicate higher-order GWs from the major core of the polar vortex jet.

We now compare the simulated and observed EPBs. Figures 10e and 10g show close-ups of the dTEC from SAMI3 over northeastern Brazil at 01:00 UT on 13 January and 00:40 UT on 14 January, respectively. The spacing of the periodic EPBs is indicated with pink arrows. Note that the horizontal spacing is somewhat larger in Figure 10e than in Figure 10g. The vertical TEC (vTEC) is computed from GNSS observations using an ionospheric pierce point of $z = 350$ km for elevation angles ≥30° and is then binned: 0.5° × 0.5° (Otsuka et al., 2002). The values are smoothed with a 10-min running average and spatially with a 1.5° × 1.5° running average. If vTEC data is not available, the running average is increased to 2.5° × 2.5° up to 10.5 ° × 10.5° (Takahashi et al., 2014, 2015). This vTEC is not detrended in time. The spatial resolution is ~50–100 km in southeastern Brazil and ~200–300 km in northeastern Brazil (Takahashi et al., 2016). Figures 10f and 10h shows the resulting observed vTEC over Brazil at 01:00 UT on 13 January and 00:40 UT on 14 January, respectively. The EPBs are observed at similar locations and have similar horizontal spacings as the EPBs simulated by SAMI3.

6. Waves Observed in the Ionosphere, and Comparison With Model Results

GWs generate TIDs through ion-neutral collisions (e.g., Hocke & Schlegel, 1996). We now present observations of waves in the D, E, and F regions of the ionosphere, and compare them with the simulated GWs and TIDs. We do not compare with the simulated TIDs at >60°N due to the lower resolution of SAMI3 there. Figure 11 shows the Kp and Ap on 9–20 January 2016. Mild geomagnetic activity with Kp ~ 3–4 occurred at 12 UT on 11 January

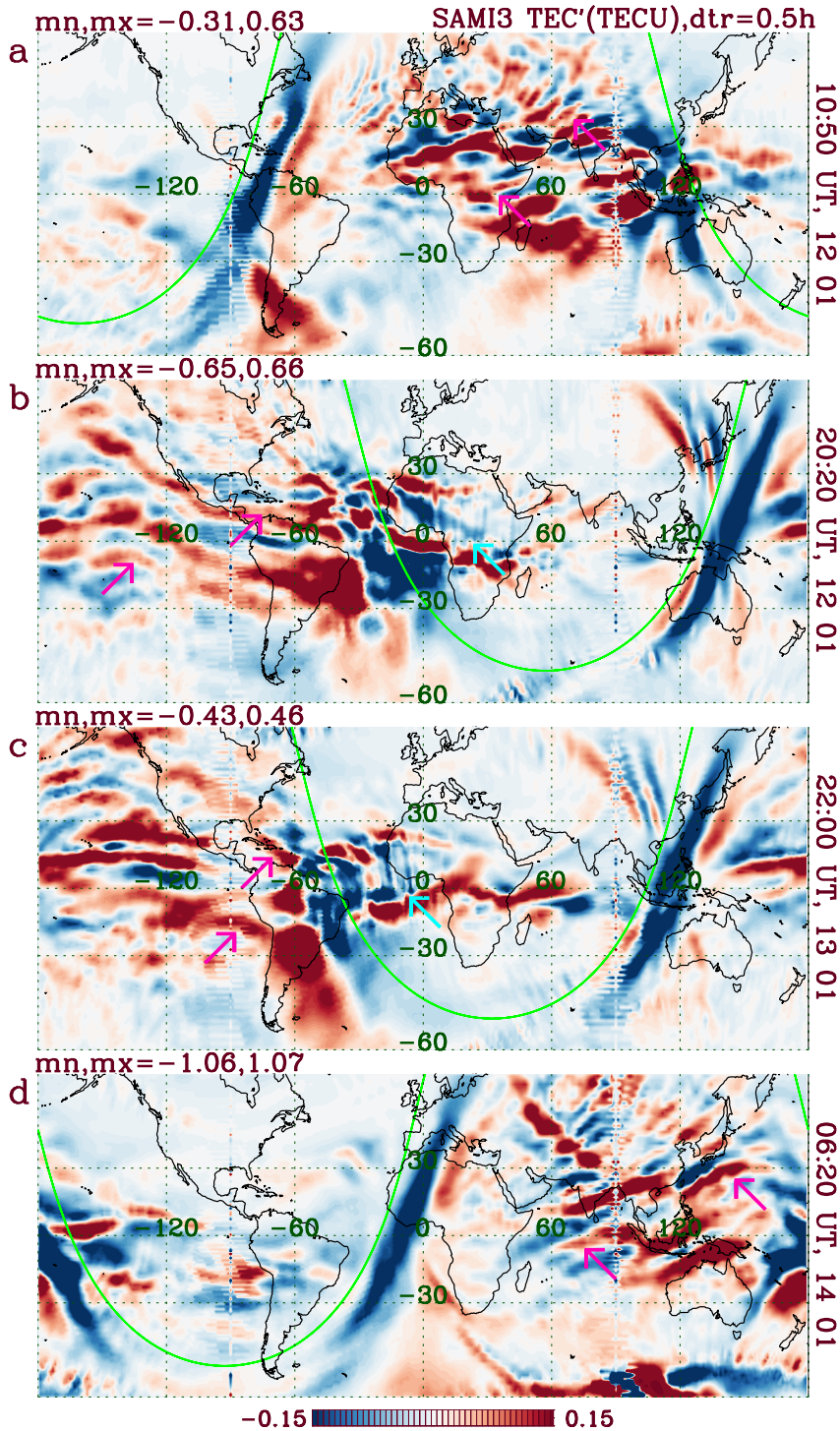

Figure 9. dTEC (colors, in TECU) from the SAMI3 using a 30-min detrend window at (a) 10:50 UT on 12 January 2016, (b) 20:20 UT on 12 January, (c) 22:00 UT on 13 January, (d) 6:20 UT on 14 January. Pink arrows indicate TIDs generated by higher-order GWs from the polar vortex jet. Turquoise arrows indicate EPBs in (b and c). Minimum and maximum values are given at the top of each panel. Green solid lines show the sunrise and sunset solar terminators. The colors are oversaturated to see the TIDs.

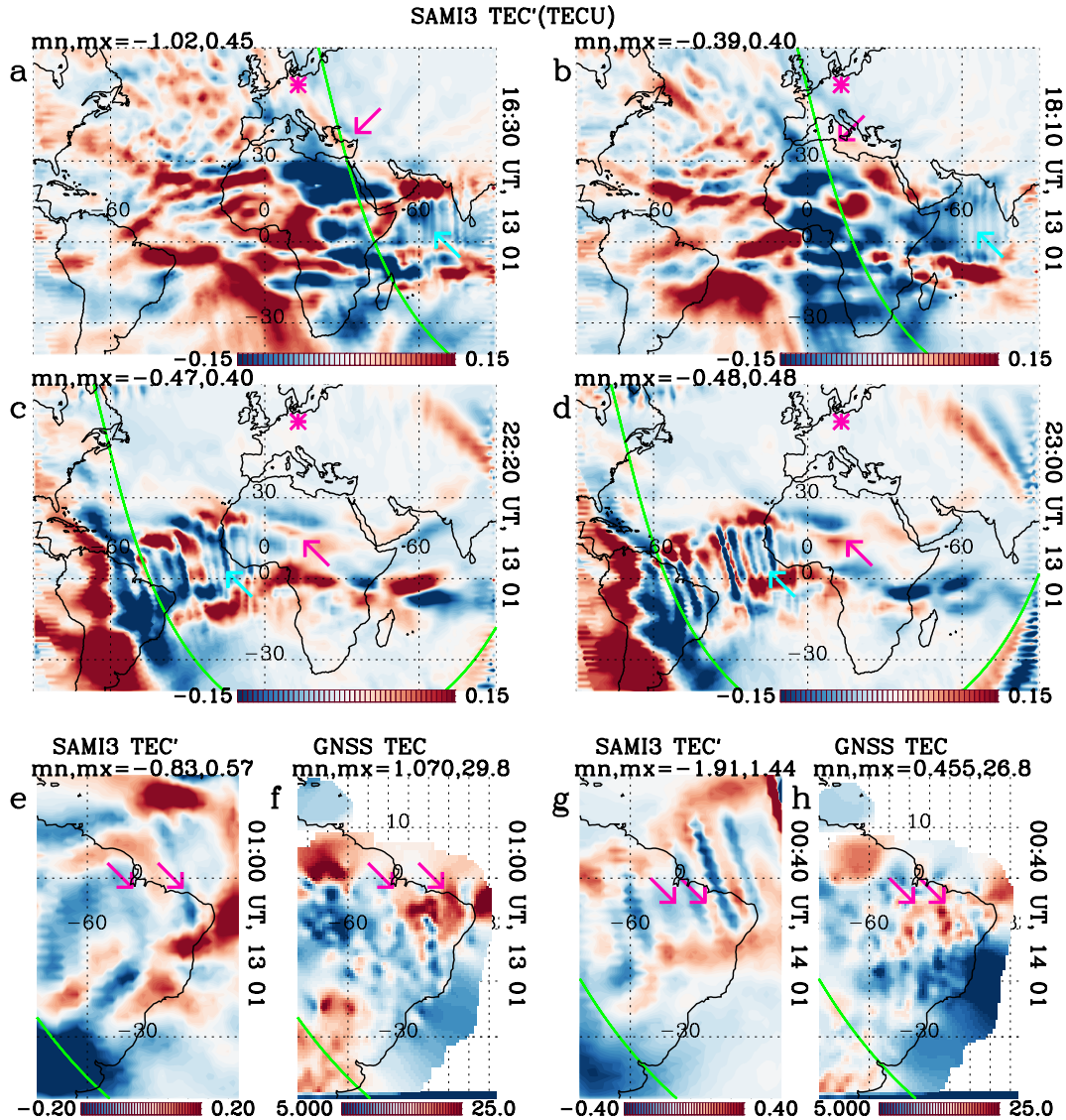

Figure 10. dTEC (colors, in TECU) from the SAMI3 using a 30-min detrend window on 13 January 2016 at 16:30 UT (a), 18:10 UT (b), 22:20 UT (c) and 23:00 UT (d). In panels (a)–(d), pink asterisks indicate (13°E, 52°N), turquoise arrows indicate the EPBs, and pink arrows indicate higher-order GWs from the polar vortex jet. (e) Close-up of dTEC from SAMI3 over northeastern Brazil at 01:00 UT on 13 January using a 30-min detrend window. Pink arrows indicate the EPB spacing. (f) Observed vTEC from GNSS at the same time as (e). Pink arrows are in same locations as (e). (g)–(h) Same as (e)–(f) but at 00:40 UT on 14 January. Minimum and maximum values are given at the top of each panel. Green solid lines show the sunrise and sunset solar terminators. The colors are oversaturated to see the TIDs and EPBs.

through 0 UT on 12 January and at 12 UT on 12 January through 6 UT on 13 January. Otherwise, Kp < 3 throughout the study period.

6.1. TIDs Observed by the EISCAT VHF Radar at Tromsø, Norway

In this section we examine the TIDs in the D, E, and F regions observed by the Very High Frequency (VHF) EISCAT (European Incoherent Scatter Scientific Association) radar at Tromsø in Norway (69.58°N 19.23°E).

6.1.1. TIDs in the D and E Regions of the Ionosphere

Figure 12a shows $\log_{10}(N_e)$ every minute measured by the VHF EISCAT radar at Tromsø on 15 January 2016 using the "manda" mode. Here, N_e is the electron density. We have applied a 2D running mean that is 30 min in

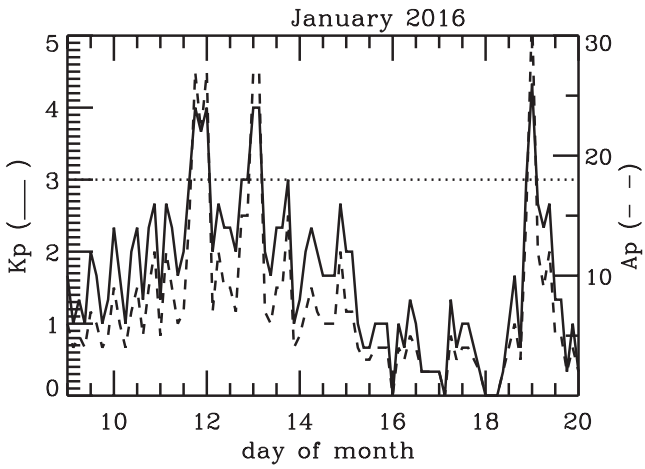

Figure 11. Kp (solid line) and Ap (dash line, right *y* axis) from Matzka et al. (2021) during 9–20 January 2016. The dotted line shows Kp = 3.

time and 2.8 km in z. The manda mode is specifically designed for greater sensitivity at low altitudes and much higher vertical resolution than other EISCAT experiments, such as bella. This mode has a vertical resolution of 0.36 km up to 110 km, with the resolution decreasing from 3 to 10 km at $z \geq 110$ km. During the summer, this mode can achieve reliable sounding of the D region ionosphere down to $z = 60$ km; however, with the lower densities in the winter, sensitivity is more typically limited to $z \geq 70$ km. Perturbations in N_e are seen at $z \sim 60-80$ km in Figure 12a. The yellow dash line at $z = 75$ km delineates the altitude range ($z \geq 75$ km) where we have full confidence in the data. Figure 12b shows $N_e'/\overline{N_e}$ for waves with 15 min $< \tau <$ 1.6 hr, where $\overline{N_e}$ is the background electron density. Here we have applied a 2D running mean that is 30 min in time and 2.8 km in z in order to better compare with the HIAMCM GWs. Waves with upward and downward phases in time are seen, indicating possible downward and upward-propagating GWs, respectively. Importantly, a likely long-lasting fishbone structure is seen at ~5–9 UT with a "knee" (altitude where the horizontally-displaced LBF generates the secondary GWs) at $z_{\text{knee}} \sim 80$ km, as indicated by the green arrows. Figure 12c shows w' from the HIAMCM detrended to include GWs with $\tau < 1.6$ hr. Because the HIAMCM results we display here are recorded every 10 min with $\Delta z = 1$ km at $z \sim 70-120$ km, the displayed GWs have $\tau \geq 30$ min and $|\lambda_z| \geq 3$ km. (This is why we applied a running mean smoothing to the data of 30 min/2.8 km in Figures 12a and 12b.) The long-lasting fishbone structure is also seen at 5 – 9 UT (green arrows). Good agreement between the simulated and observed fishbone structures is seen in Figures 12b and 12c. Thus, it is possible that GWs may, in part, define the lower side of the D region of the ionosphere.

Figures 12d and 12e shows the corresponding EISCAT data on 16 January. Upward and downward-propagating waves are seen, with possible fishbone structures occurring at ~5–9 UT at $z_{\text{knee}} \sim 80-85$ km (green arrows). Unfortunately HIAMCM results are not available on 16 January.

6.1.2. TIDs in the F Region of the Ionosphere

Figure 13a shows the electron density N_e measured by the VHF EISCAT radar at Tromsø on 11 January 2016 using the "bella" mode. We only show the results in the F region at $z \geq 150$ km due to the low sensitivity of the bella mode at lower altitudes. Figure 13b shows $N_e'/\overline{N_e}$, where N_e' contains waves with $\tau = 30$ min to 3 hr, and the background electron density $\overline{N_e}$ is obtained by removing waves with $\tau < 4$ hr. During this bella run, particle precipitation is seen throughout much of the period from 0UT to 7UT and 17UT on, with the first period mainly composed of diffuse auroral precipitation and the evening having a mix of diffuse auroral precipitation, discrete arcs, and F-region plasma patches; as such, we will focus here on daytime hours in the F region. Figure 13c shows the vertical velocity w from the HIAMCM for GWs with $\lambda_H < 2001$ km. Here, the HIAMCM results are sampled at the same locations and times as the EISCAT data in Figure 13b. Comparing Figures 13b and 13c, many of the TIDs and GWs have similar τ and λ_z at ~1–12 UT. We indicate several of these waves with green arrows. N_e' and w' are often ~90° out of phase. If chemistry can be neglected, the ion velocity generally lags 90° behind N_e' at the bottomside of the F layer (Vadas & Nicolls, 2009). At this high latitude location, the ion velocity is mainly composed of w'. Thus N_e' is expected to lag 90° behind w' when chemistry can be neglected. This is approximately true for GWs at $z \sim 180$ km and ~10 UT (green arrows). As expected, the TIDs do not follow the GWs at 12–24 UT due to particle precipitation. Note that the GW $|\lambda_z|$ is much larger at night than during the day in Figure 13c. Over ALOMAR, most of the thermospheric GWs propagate northward, away from the approximate concentric ring center at (~13 – 15°E, ~52 – 53°N) (see pink asterisks in Figures 6 and 7a–7d). During the night (day), the thermospheric wind is southward (northward) over ALOMAR. Thus, the thermospheric GWs over ALOMAR propagate against the wind at night and with the wind during the day, resulting in larger (smaller) $|\lambda_z|$ at night (day).

Figure 14a shows the corresponding results on 12 January 2016. Many of the TIDs and GWS at 0–13 UT have similar τ and λ_z, as indicated by the green arrows. After 13 UT, the TIDs do not follow the GWs due to geomagnetic activity. Thus, τ and λ_z of the modeled GWs agree well with that of the TIDs observed by EISCAT during 1–12 UT on 11 January and 7–13 UT on 12 January (quiet-times) at $z > 150$ km.

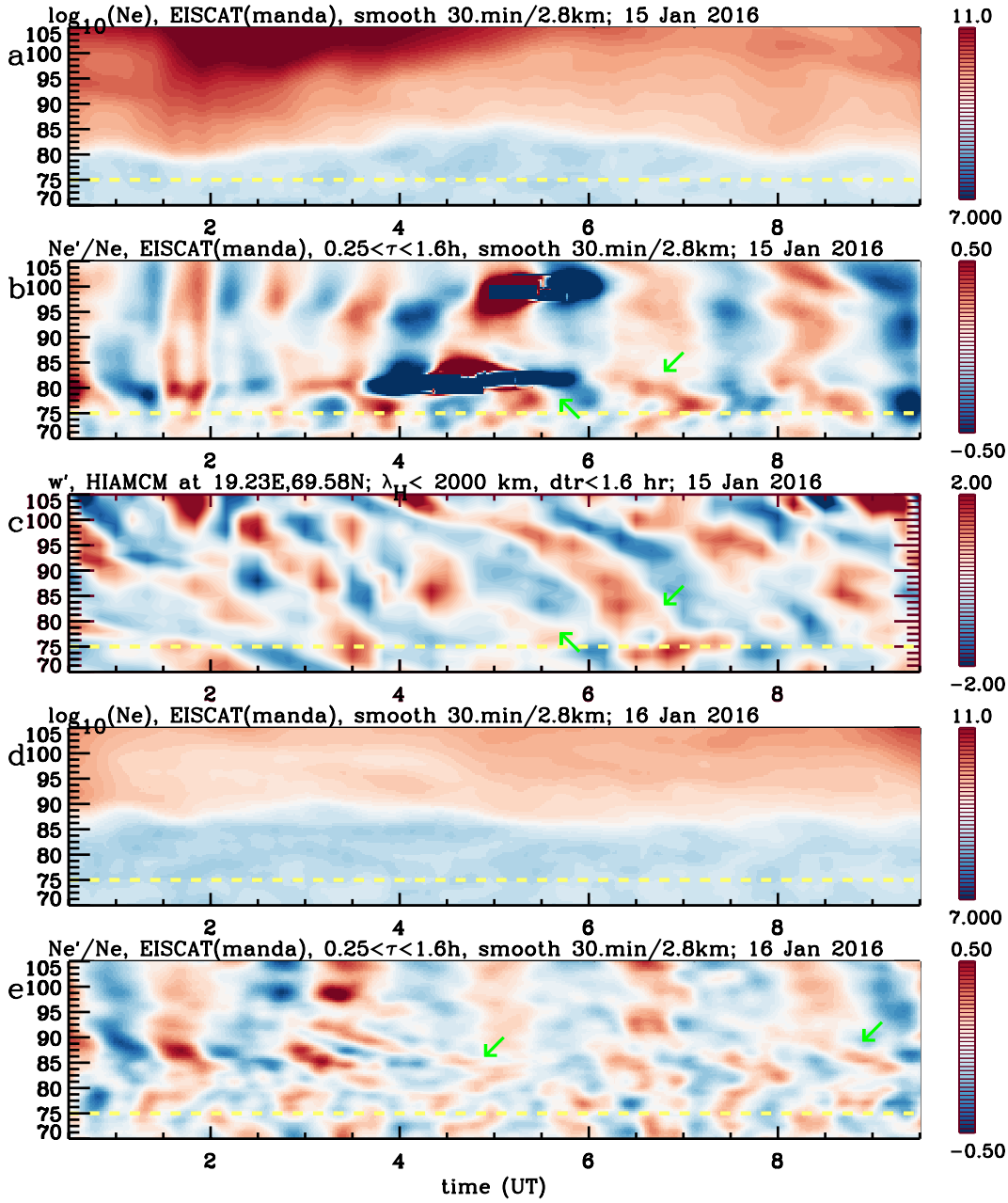

Figure 12. (a) $\log_{10}(N_e)$ every minute as functions of altitude and time on 15 January 2016 measured by the VHF radar at EISCAT Tromsø, Norway in "manda" mode. N_e is in m^{-3}. (b) $N_e'/\overline{N_e}$, where the prime includes waves with 15 min to 1.6 hr. A 2D running mean is applied for 30 min in time and 2.8 km vertically for (a)–(b). (c) w' from the HIAMCM at Tromsø for GWs with $\lambda_H < 2001$ km and $\tau < 1.6$ hr. The green arrows in (b)–(c) indicate a fishbone structure; these arrows are in the same locations in (b)–(c). (d)–(e): Same as (a)–(b) but on 16 January. The yellow dash lines (at $z = 75$ km) delineate the lower boundary ($z \geq 75$ km) where we have full confidence in the data.

6.2. PFISR Observations of TIDs

TIDs generated by GWs have been investigated using the Poker Flat Incoherent Scatter Radar (PFISR) (Nicolls & Heinselman, 2007; Vadas & Nicolls, 2008), including TIDs generated by higher-order GWs from orographic forcing (Vadas & Nicolls, 2009). PFISR is located at 147.47°W and 65.13°N in Alaska. We obtain N_e from PFISR at 18 UT on 14 January through 4 UT on 15 January 2016. During this time, PFISR measured N_e in 4 beams. Figure 15a shows the locations of these beams at $z = 200$ km. We use a cutoff period of 3.5 hr and a cutoff

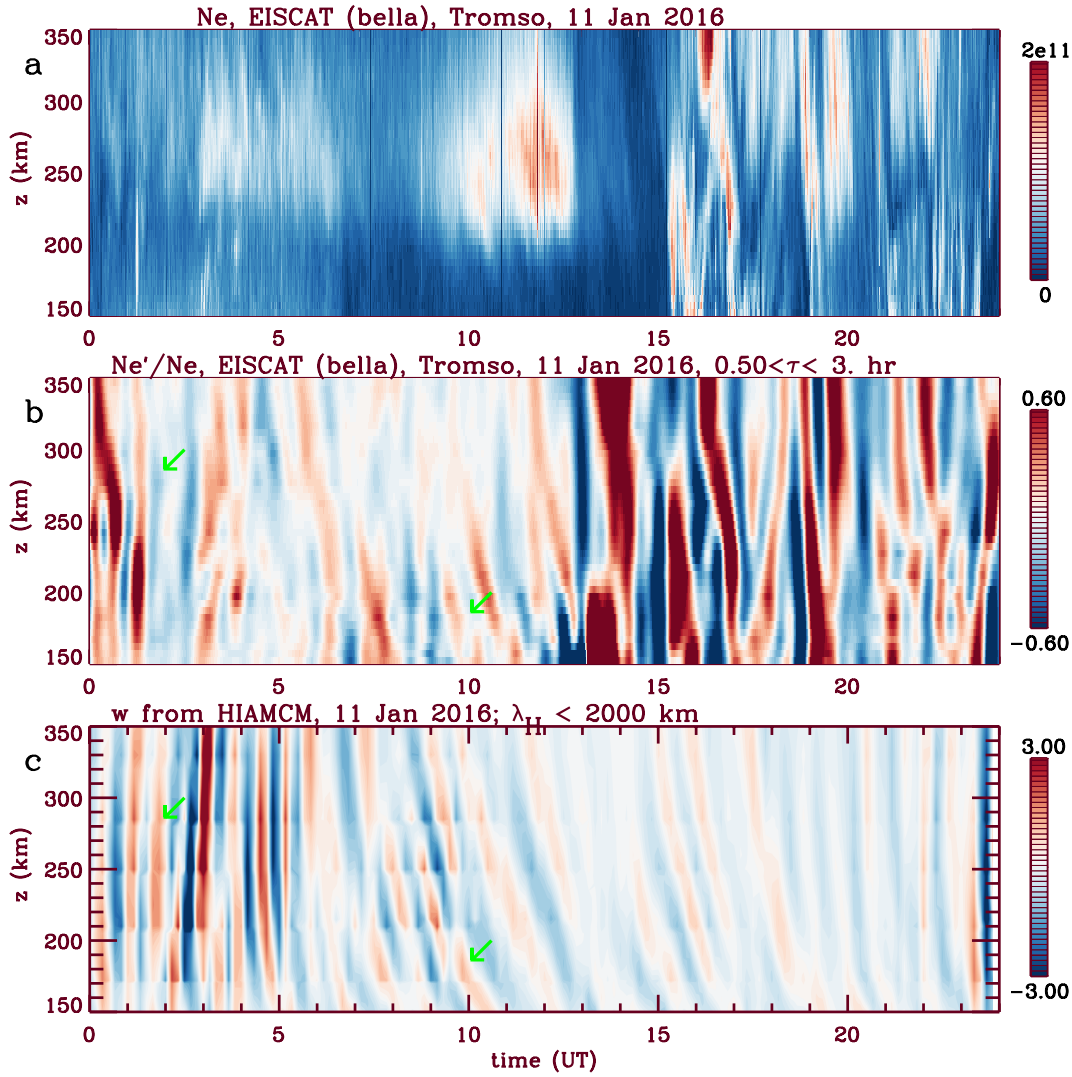

Figure 13. (a) Total electron density N_e (in m^{-3}) as functions of altitude and time from the EISCAT radar at Tromsø, Norway (located at 69°35'N, 19°13'E) on 11 January 2016 using the "bella" mode. (b) $N_e'/\overline{N_e}$ as functions of altitude and time for τ_r = 30 min to 3 hr, where $\overline{N_e}$ is the background electron density after removing wave perturbations with $\tau_r < 4$ h from (a). (c) w (in m/s) from the HIAMCM sampled at the same locations and times as the EISCAT data in panel (b). The green arrows in panels (b) and (c) are in the same locations.

vertical wavelength of 120 km to obtain the background $\overline{N_e}$. To calculate the electron density perturbations N_e' that could be generated by higher-order GWs, we subtract the background from N_e, then remove waves with $\tau < 20$ min and $|\lambda_z| < 20$ km. Figure 15b shows $\overline{N_e'/\overline{N_e}}$ for each beam, where $\overline{N_e'/\overline{N_e}}$ is averaged over z = 180–200 km. During 19.5–22 UT, the TIDs have $\tau \sim 40-60$ min with little amplitude variation between the beams (other than a temporal offset), which suggests that these TIDs are generated by a GW that is "passing through" rather than by auroral activity. (During 22–24 UT, however, there is significant variability of N_e' among the beams, which suggests possible auroral activity.) During 20–21.2 UT, the TIDs first reach beam 3, then beams 1 and 4 approximately simultaneously, then beam 2; therefore, these TIDs propagate southeastward. Figure 15c shows $\overline{w}$, which is the vertical velocity w from the HIAMCM averaged from z = 180–200 km. GWs with $\tau \sim$ 40–80 min occur during 19.5–24 UT. Although there are several GW packets, the main GW packet propagates southeastward as well, since the largest-amplitude GWs reach beam 3 first and beam 2 last. Therefore, τ and the propagation direction of the observed TIDs agree well with that of the simulated GWs. Figures 15d–15g shows $N_e'/\overline{N_e}$ from PFISR for beams 1–4, and Figures 15h–15k shows w from the HIAMCM sam beams 1–4. The observed TIDs have similar τ and λ_z as the simulated GWs during 20–23 UT. (Auroral activity is apparent in

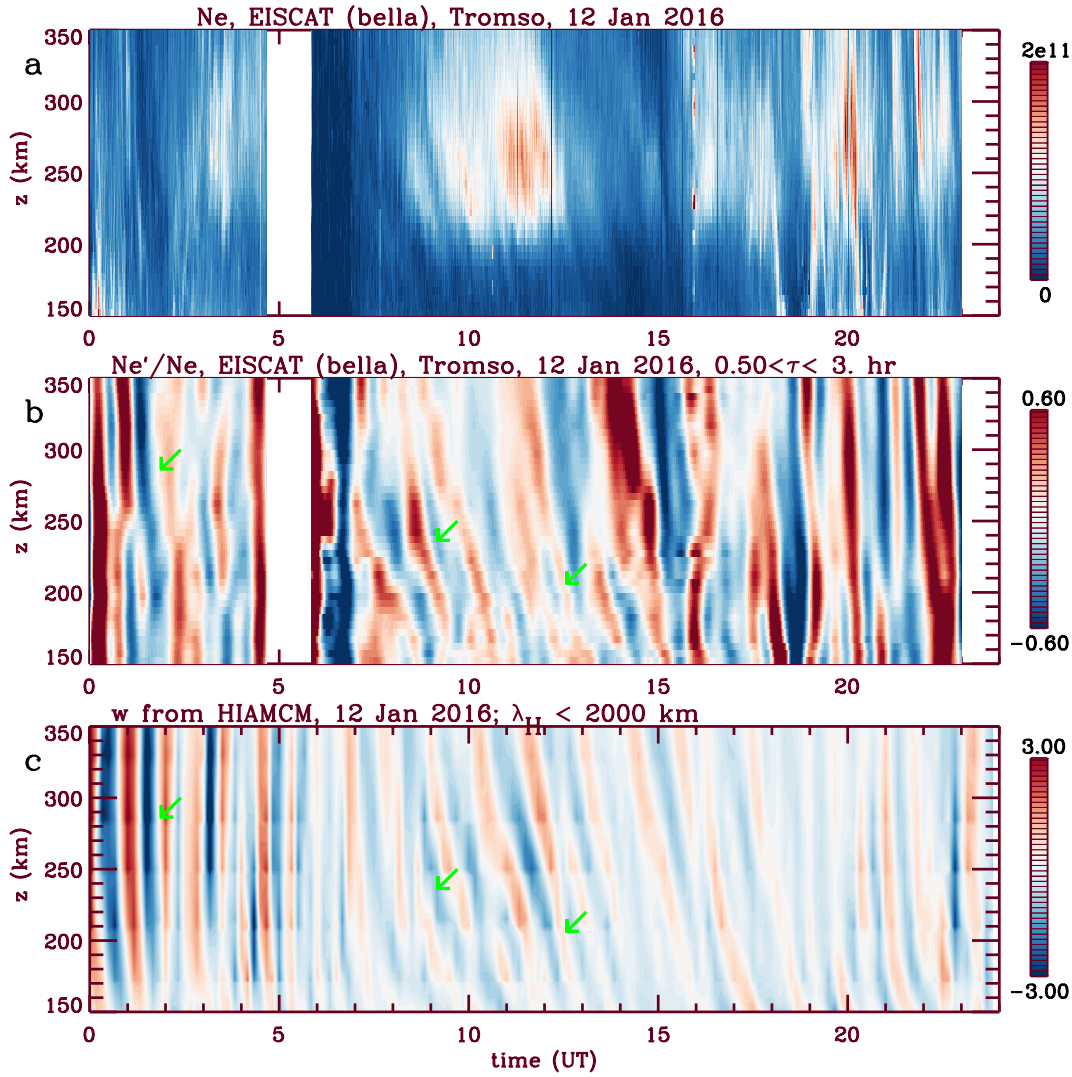

Figure 14. Same as in Figure 13 but on 12 January 2016.

Figures 15d–15g after 23 UT.) These simulated GWs were shown in Figures 7e–7h (turquoise asterisks indicate the location of PFISR in those panels), and are part of a larger GW packet that propagated southeastward across PFISR and the CONUS (pink arrows) from northeastern Asia (pink asterisks). Therefore, it is likely that the TIDs observed by PFISR at ~20–23 UT were generated by higher-order GWs from the exit/entrance region of the polar vortex jet.

6.3. GNSS Observations of TIDs

TIDs generated by GWs have been investigated using GNSS observations (e.g., Azeem et al., 2015; Nishioka et al., 2013). Here we obtain slant TEC (sTEC) data from GNSS receivers from the Madrigal database, from the Crustal Dynamics Data Information System (CDDIS) (as in Themens et al. (2022)), Dr. Grzegorz Nykiel's Polish data set, the National Land Survey of Finland's positioning service (FINPOS), the Quebec Geodetic Service, and the NERC British Isles continuous GNSS Facility. We then compute the differential vertical TEC (dTEC) for a given Ionospheric Pierce Point (IPP) altitude of z_{IPP} (e.g., Mrak et al., 2021; Themens et al., 2022; Vierinen et al., 2016).

Most researchers assume $z_{\mathrm{IPP}} = 280{-}350$ km when calculating the dTEC; however this altitude is too high for many GWs because they dissipate from the exponentially-increasing kinematic viscosity and thermal diffusivity. In fact, a GW's dissipation altitude, z_{diss}, depends strongly on λ_z and c_{IH}. For example, a GW with $\lambda_H = 300$ km

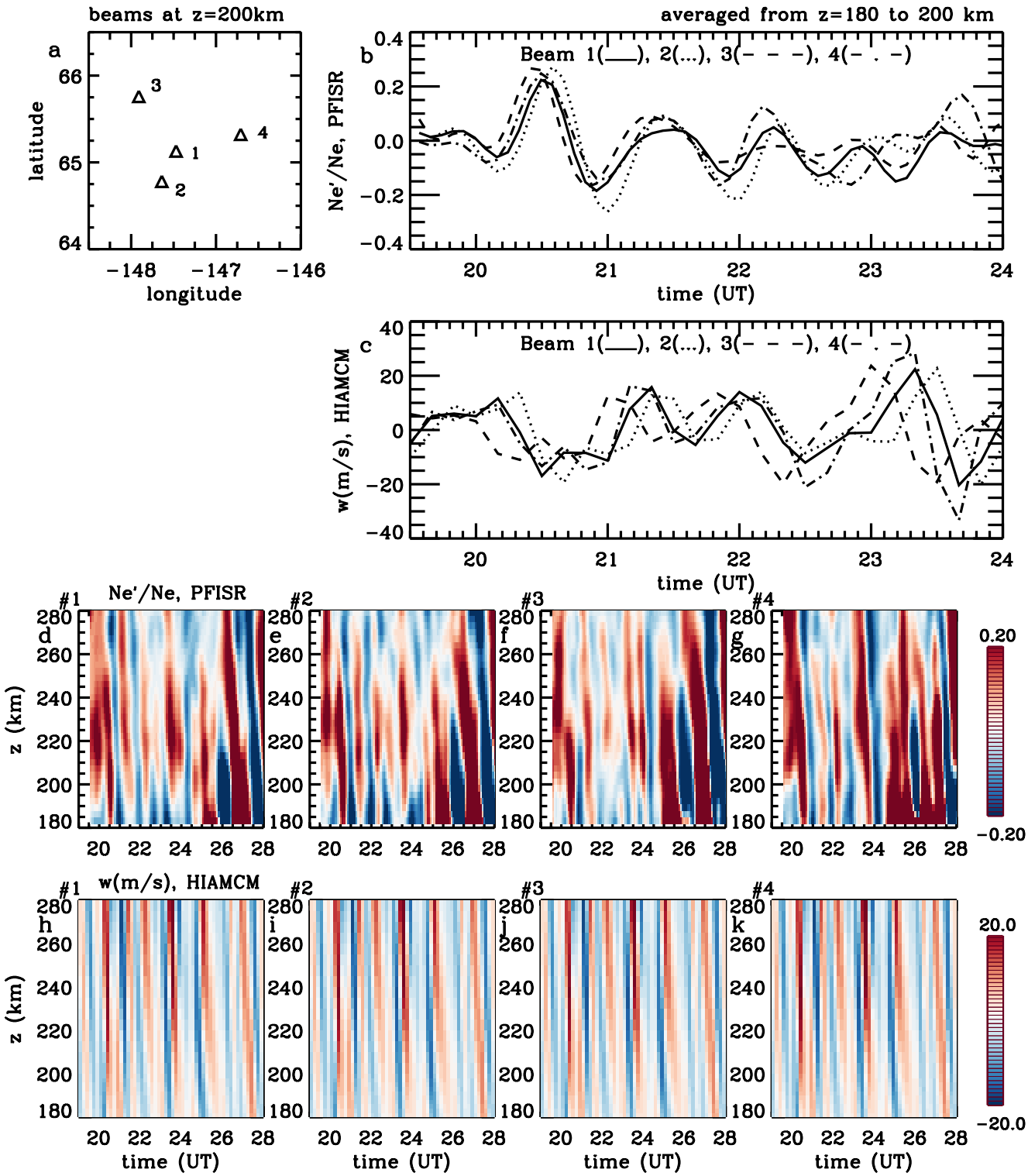

Figure 15. (a) Beam locations at $z = 200$ km for the Poker Flat Incoherent Scatter Radar (PFISR) on 14–15 January 2016. (b) $\overline{N_e'/N_e}$ for TIDs with $\tau > 20$ min and $|\lambda_z| > 20$ km for beams 1–4 as solid, dot, dash and dash-dot lines, respectively. The values are averaged from $z = 180$ to 200 km. (c) $\overline{w}$ from the HIAMCM along beams 1–4 (solid, dot, dash and dash-dot lines, respectively), where w is averaged from $z = 180$–200 km. (d)–(g): $N_e'/\overline{N_e}$ observed by PFISR for TIDs with $\tau > 20$ min and $|\lambda_z| > 20$ km for beams 1–4, respectively. (h)–(k): w from the HIAMCM along beams 1–4, respectively.

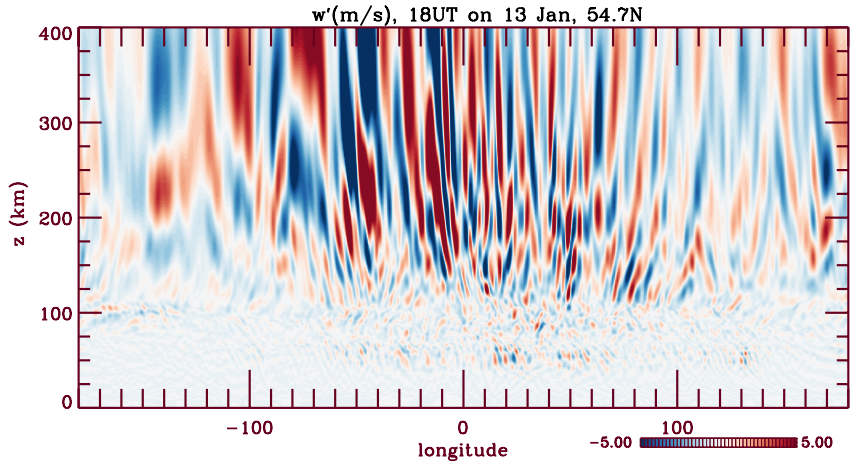

Figure 16. The longitude-vertical slice of w' (colors, in m/s) at 54.7°N for GWs from the HIAMCM with $\lambda_H < 2001$ km at 18 UT on 13 January 2016.

and intrinsic period $\tau_{Ir} = 30$ min has its maximum amplitude at $z_{\text{diss}} \sim 170–190$ km, while one with $\lambda_H = 400$ km and $\tau_{Ir} = 20$ min has $z_{\text{diss}} \sim 250–325$ km (Figures 4 and 6 of Vadas, 2007). Above z_{diss}, a GW's amplitude decreases rapidly in z. Thus many GWs dissipate well below the F peak. Typical altitudinal profiles of dissipating GWs are shown in Fig. 4 of Vadas and Nicolls (2012). As an example, Figure 16 shows a longitude-vertical slice of w' at 54.7°N for GWs from the HIAMCM with $\lambda_H < 2001$ km at 18 UT on 13 January 2016 during our case study. Although the medium-scale GWs have relatively large amplitudes at $z \sim 200$ km, most dissipate from $z \sim 200$ to 300 km. Since a TID generated by a GW is not self-sustaining, the TID disappears when the GW dissipates (Nicolls et al., 2014; Vadas & Nicolls, 2009). Thus the altitude which contains the largest contribution to the dTEC from a GW depends on both z_{diss} and $N_e(z)$. The issue that $z_{\text{IPP}} \sim 350$ km may be too high when studying GWs/TIDs was first discussed by Ozeki and Heki (2010). They noted that if z_{IPP} is too high, misalignment between the TID wavefronts can occur, especially when the TIDs are observed by different GNSS satellites.

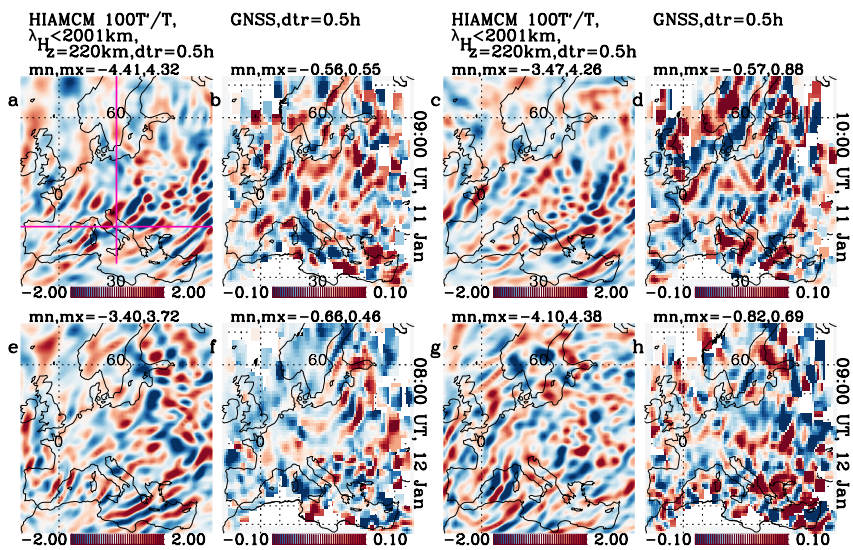

Figure 17. Horizontal slices of the GWs and TIDs over Europe. (a) $100T'/\overline{T}$ (colors) from the HIAMCM at $z = 220$ km for GWs with $\lambda_H < 2001$ km on 11 January 2016 at 9:00 UT. The pink lines show 15°E and 42.5°N as well as the longitude and latitude ranges used for the keograms shown in Figures 18 and 19, respectively. (b) Observed dTEC (colors, in TECU) on 11 January at 9:00 UT. Panels (a) and (b) are detrended with a 30-min running window. Same as panels (a) and (b) but at 10:00 UT on 11 January (c) and (d), 8:00 UT on 12 January (e) and (f), and 9:00 UT on 12 January (g) and (h). The colors are oversaturated to emphasize the waves.

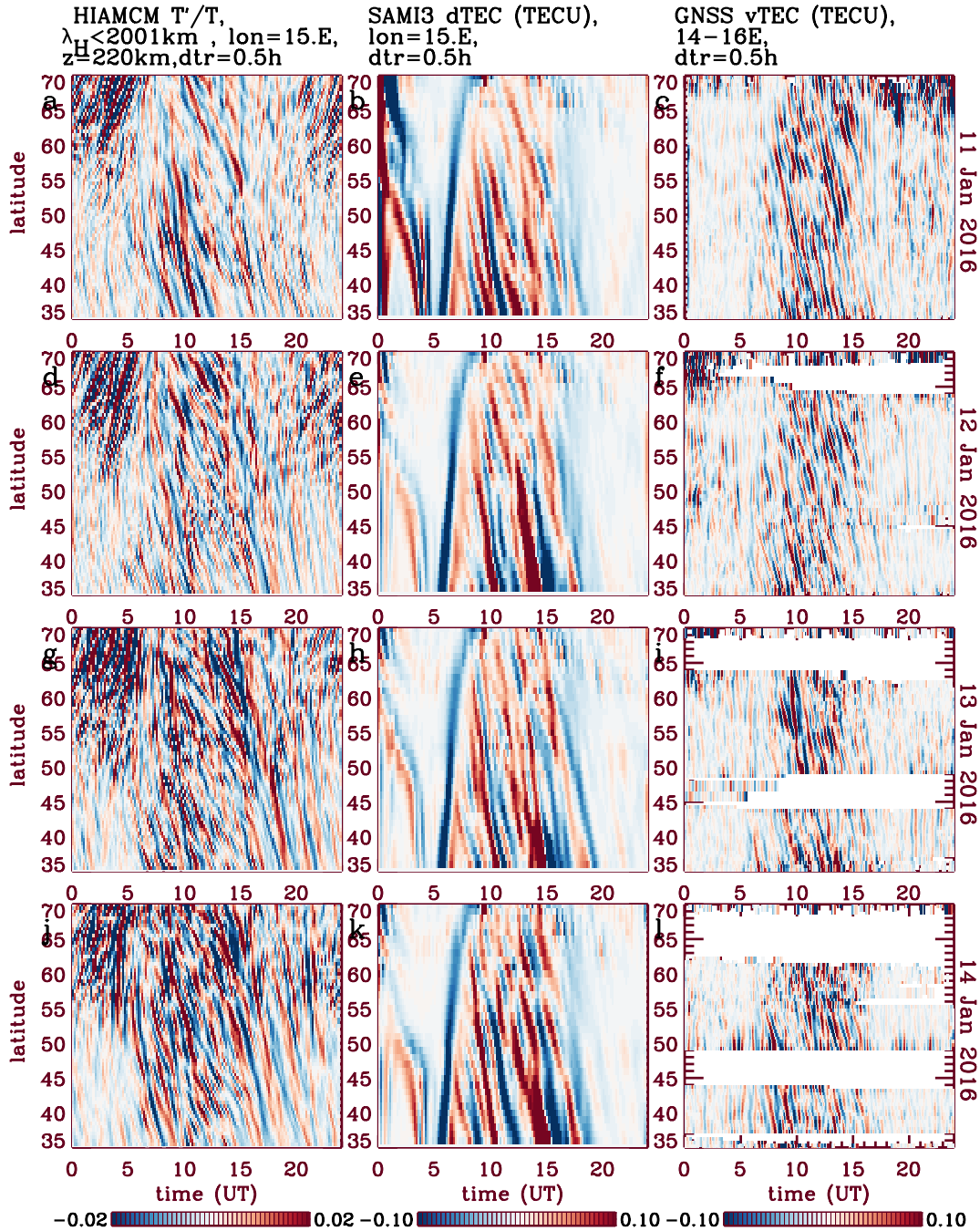

Figure 18. Keograms of the GWs and TIDs vs. latitude over Europe. (a) Keogram of $T'/\overline{T}$ from the HIAMCM on 11 January 2016 at 15°E for GWs with $\lambda_H < 2001$ km at $z = 220$ km. The results are detrended with a 30-min running window. (b) Keogram of dTEC (in TECU) from SAMI3 using a 30-min detrend window on 11 January 2016 at 15°E. (c) Keogram of dTEC (in TECU) from GNSS on 11 January 2016 averaged from 14 − 16°E using a 30-min detrend window. Rows 2–4: Same as row 1 but on 12–14 January 2016, respectively. The colors are oversaturated to emphasize the waves.

Here, we assume $z_{\mathrm{IPP}} = 220$ km in order to account for typical values of z_{diss} for GWs propagating in the region of the thermosphere which overlaps with the F region. We obtain the corrected sTEC from 6378 GNSS stations and 32 satellites worldwide (after first order receiver and satellite biases are removed). We then detrend the corrected sTEC with a 30-min running mean. Finally, we convert the detrended sTEC to dTEC assuming $z_{\mathrm{IPP}} = 220$ km for observations with elevations ≥30°.

6.3.1. GWs and TIDs Over the European Sector

We first compare horizontal maps of the simulated GWs with the observed TIDs. The first and third columns of Figure 17 show $100T'/\overline{T}$ at $z = 220$ km from the HIAMCM for GWs with $\lambda_H < 2001$ km at various times during 11–12 January over Europe. The maps are detrended with a 30-min running window. Medium to large-scale GWs with arc-like and planar wave structures are seen. The second and forth columns show the observed dTEC from GNSS at the same times. These maps are created by binning the dTEC into $0.5° \times 0.5° \times 1$ min bins and smoothing with a $1.5° \times 1.5°$ running mean. MSTIDs with arc-like and planar wave structures are seen. Reasonably good agreement is occasionally seen between the simulated GWs and observed MSTIDs in terms of the morphology of the wave structures and λ_H (e.g., the southeastward propagating GWs and MSTIDs over Europe at 9:00 UT on 11 January in Figures 17a and 17b, and the concentric ring/arc-like structures south of Sweden at 8:00 UT on 12 January in Figures 17e and 17f).

We now display keograms of the GWs and TIDs in order to estimate and compare the wavelengths and periods of the waves. Figure 18a shows a latitude-time keogram at 15°E of $T'/\overline{T}$ for GWs from the HIAMCM with $\lambda_H < 2001$ km at $z = 220$ km on 11 January. We detrend these results with a 30-min running window to highlight the medium-scale GWs. We choose this longitude because it slices through central Europe (including Tromsø). The location of this keogram is indicated by the vertical pink line in Figure 17a. Medium to large-scale GWs with $T'/\overline{T} \sim 1\%–3\%$ propagate southward (northward) during the day (night) over Europe. Figure 18b shows the corresponding keogram of the dTEC from SAMI3 using a 30-min detrend window. TIDs propagate southward during the day with TEC' $\sim 0.05–0.2$ TECU. These TIDs are mainly large scale with $\lambda_y > 800$ km and $\tau > 40$ min, where λ_y is the meridional wavelength. (This result, that SAMI3 is not able to capture MSTIDs with $\tau < 40$ min, was found for TIDs generated by GWs from the Tonga volcanic eruption (Vadas, Figueiredo et al., 2023).) The TIDs have similar characteristics as the GWs with $\tau \geq 40$ min from Figure 18a during the daytime. The sunrise terminator wave is visible at 5–7 UT (negative dTEC (blue)). Note that the sunrise terminator wave does not appear in Figure 18a because this wave has $\lambda_H \sim 3000$ km (Forbes et al., 2008). Figure 18c shows the observed dTEC averaged over $14 - 16$°E. Excellent agreement is seen between the daytime simulated GWs and observed TIDs in terms of wavelengths, periods and propagation speeds (i.e., the slopes of the phase lines). In addition, good agreement is seen between the SAMI3 and observed TIDs for $\tau > 40$ min. Rows 2–4 show the corresponding results for 12–14 January 2016. Comparing the panels, and noting that the simulated GWs are higher-order GWs "from below" (i.e., are not from geomagnetic forcing), we conclude that virtually all of the observed daytime TIDs are generated by higher-order GWs from below. This result highlights the importance of MSVC in creating wintertime MSTIDs and LSTIDs. Note: since the dTEC amplitudes simulated by HIAMCM-SAMI3 agree well with the observed dTEC amplitudes, we infer that the amplitudes of the wintertime thermospheric higher-order GWs simulated by the HIAMCM are reasonably realistic.

Figure 19a shows a longitude-time keogram at 42.2°N of $T'/\overline{T}$ for GWs from the HIAMCM with $\lambda_H < 2001$ km at $z = 220$ km on 11 January. We choose this latitude because it slices through a region of Europe where there is good GW activity and good GNSS data coverage. The location of this keogram is indicated with the horizontal pink line in Figure 17a. Medium and large-scale GWs have both eastward and westward propagation components, with a predominant westward propagation after LT noon. Figure 19b shows the corresponding dTEC keogram from the SAMI3. TIDs with $\tau > 40$ min propagate westward during the daytime at 9–15 LT, with similar structures as the GWs in Figure 19a. (As above, SAMI3 is not able to capture MSTIDs with $\tau < 40$ min.) Figure 19c shows the observed dTEC from GNSS averaged over 41−44°N. Good agreement is generally seen between the simulated GWs and observed TIDs during the daytime. Rows 2–4 show the corresponding results for 12–14 January 2016. Good agreement is generally seen between the simulated GWs and observed TIDs during the daytime.

6.3.2. GWs and TIDs Over North and Central America

Figure 20 compares horizontal slices of the simulated GWs at $z = 220$ km and the observed TIDs at 18 UT on 11 January, 1 and 2 UT on 12 January, and 1 UT on 13 January over North and Central America. Good agreement is generally seen for λ_H and the propagation directions of the GWs and TIDs. We note that Figures 20e and 20g show the simulated GWs at the same times as in Figures 7a, 7b and 7c, 7d, respectively. As discussed above, these are southwestward-propagating, higher-order GWs from the polar vortex jet which propagate across the Arctic then southwestward across North America. Therefore, the good agreement between the simulated GWs and observed

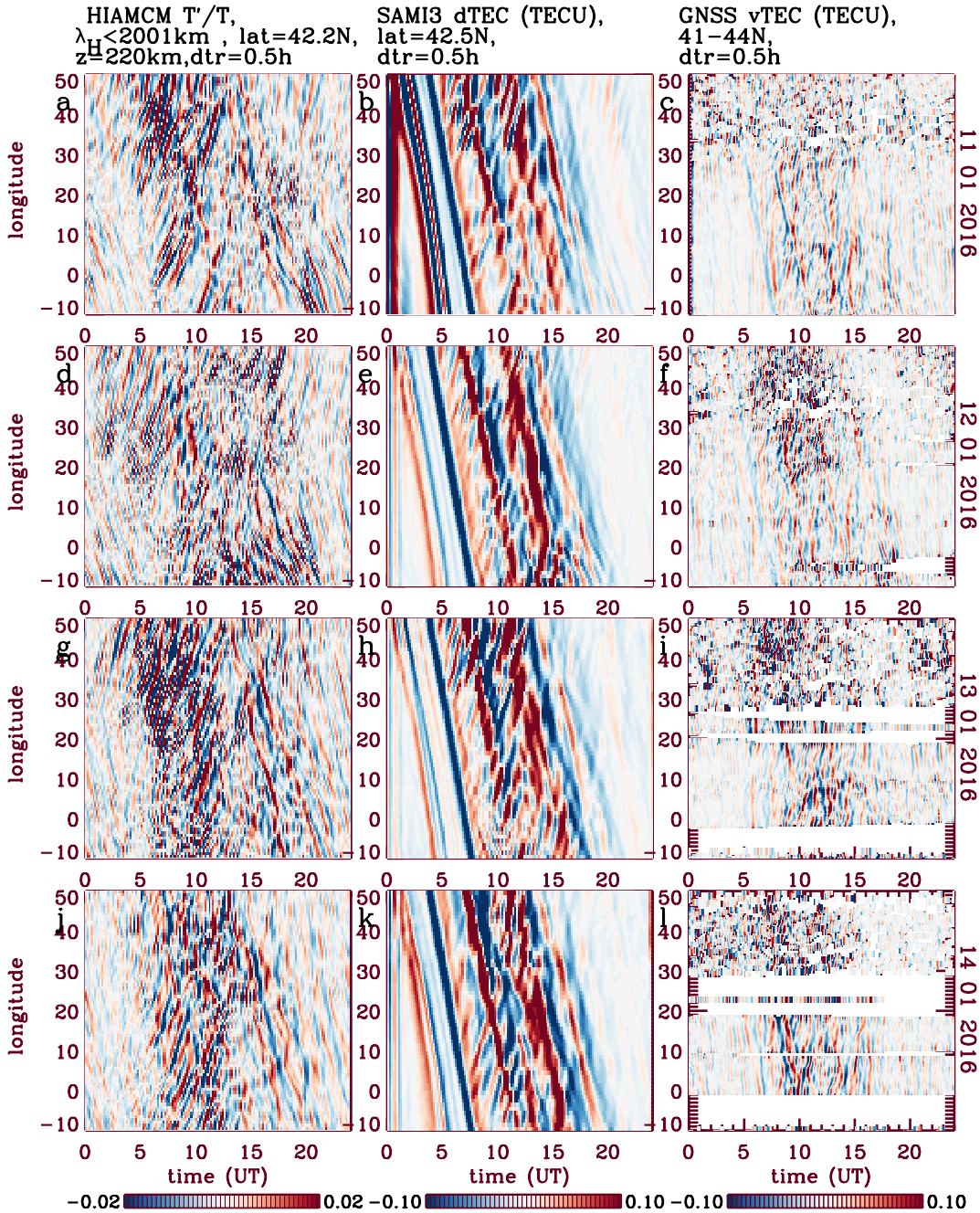

Figure 19. Keograms of the GWs and TIDs versus longitude over the European sector. (a) Keogram of $T'/\overline{T}$ from the HIAMCM for GWs with $\lambda_H < 2001$ km on 11 January 2016 at 42.2°N at $z = 220$ km. The results are detrended with a 30-min running window. (b) Keogram of dTEC from SAMI3 on 11 January 2016 at 42.5°N using a 30-min detrend window. (c) Keogram of dTEC from GNSS on 11 January 2016 averaged from 41 − 44°N using a 30-min detrend window. Rows 2–4: Same as row 1 but on 12–14 January 2016, respectively. The colors are oversaturated to emphasize the waves.

TIDs shows that the HIAMCM is able to capture the MSVC dynamics involved in generating higher-order, cross-polar GWs from the polar vortex jet.

Figure 21 shows the same latitude-time keograms as in Figure 18 but at 82.5°W. We choose this longitude because it depicts a typical slice through the CONUS and has good GNSS data coverage. The location of this keogram is indicated with the vertical pink line in Figure 20a. The simulated GWs (first column) generally propagate northward during the night and southward during the day. Note that the southward-propagating GWs

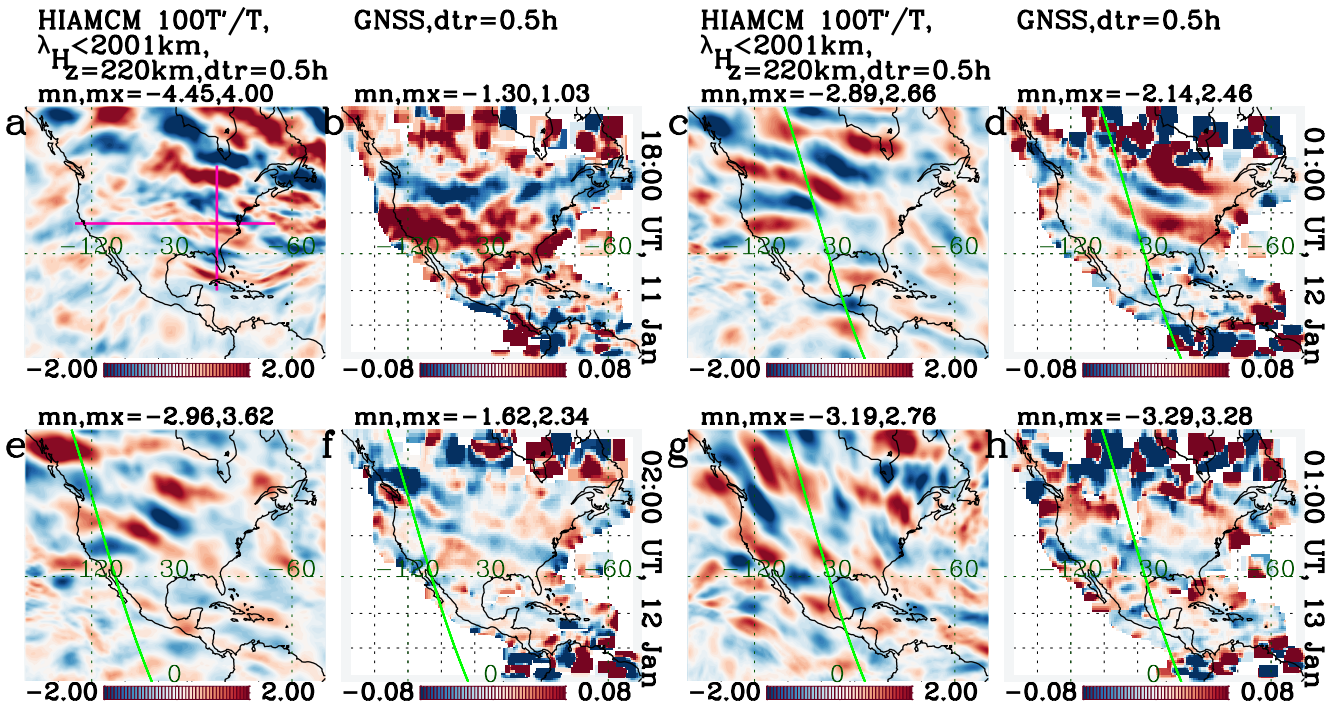

Figure 20. Horizontal slices of the GWs and TIDs over the CONUS. (a) $100T'/\overline{T}$ (colors) from the HIAMCM at $z = 220$ km for GWs with $\lambda_H < 2001$ km on 11 January 2016 at 18:00 UT. The pink lines show 82.5°W and 37.5°N as well as the longitude and latitude ranges used for the keograms shown in Figures 21 and 22, respectively. (b) Observed dTEC (colors, in TECU) on 11 January 2016 at 18:00 UT. (a)–(b) are detrended with a 30-min running window. Panels (c) and (d): same as (a) and (b) but at 1:00 UT on 12 January. Panels (e) and (f): same as (a) and (b) but at 2:00 UT on 12 January. Panels (g) and (h): same as (a) and (b) but at 1:00 UT on 13 January. The colors are oversaturated to emphasize the waves.

have much larger amplitudes than the northward-propagating GWs. The simulated TIDs from the SAMI3 (second column) are mainly LSTIDs with $\tau > 1$ hr, and mainly propagate southward during the daytime. The observed MSTIDs (third column) generally propagate southward during the daytime. Reasonably good agreement is seen between τ and the latitudinal wavelengths of the simulated GWs and the observed MSTIDs during the daytime.

Figure 22 shows the same longitude-time keograms as in Figure 19 except at 37.5°N over the CONUS. We choose this latitude because it depicts a typical slice through the CONUS and contains good GNSS data coverage. The location of this keogram is indicated with the horizontal pink line in Figure 20a. The simulated GWs (first column) generally propagate westward at 0–12 UT and eastward at 12–24 UT. The simulated TIDs (second column) generally propagate westward during the day. The observed MSTIDs (third column) generally have a similar morphology as the simulated GWs. Often when the GWs and TIDs are stationary in longitude, they instead propagate meridionally (see Figure 21). Reasonably good agreement is often seen between τ and the longitudinal wavelengths of the simulated GWs and observed TIDs. However, note that some of the observed TIDs on 11–12 January are stationary in longitude and latitude at ∼35–50°N (compare with Figure 21). These TIDs may be caused by geomagnetic activity, since Kp > 3 on those days (see Figure 11).

6.3.3. Observed TIDs in the Northern Hemisphere

We now show the observed TIDs in the Northern hemisphere during our 4-day study period. Movie S2 shows the observed dTEC at 140°W to 50°E during 11–14 January 2016 every 5 min. The data is processed as in Figures 17 and 20. In addition, the maps are smoothed with a 5 min running mean in time at each longitude/latitude to filter out high frequency noise. The propagation direction of the MSTIDs generally rotates clockwise in the anti-windward direction of the diurnal tide. The MSTIDs propagate away from Europe during most times, often with partial concentric ring/arc-like structure. Examples occur at ∼10–13 UT on 11 January, when arc-like MSTIDs propagate southward away from Norway/Sweden, and at 12:15–13:00 UT on 13 January, when concentric MSTIDs propagate southward away from southern Sweden. Often multiple centers of concentric

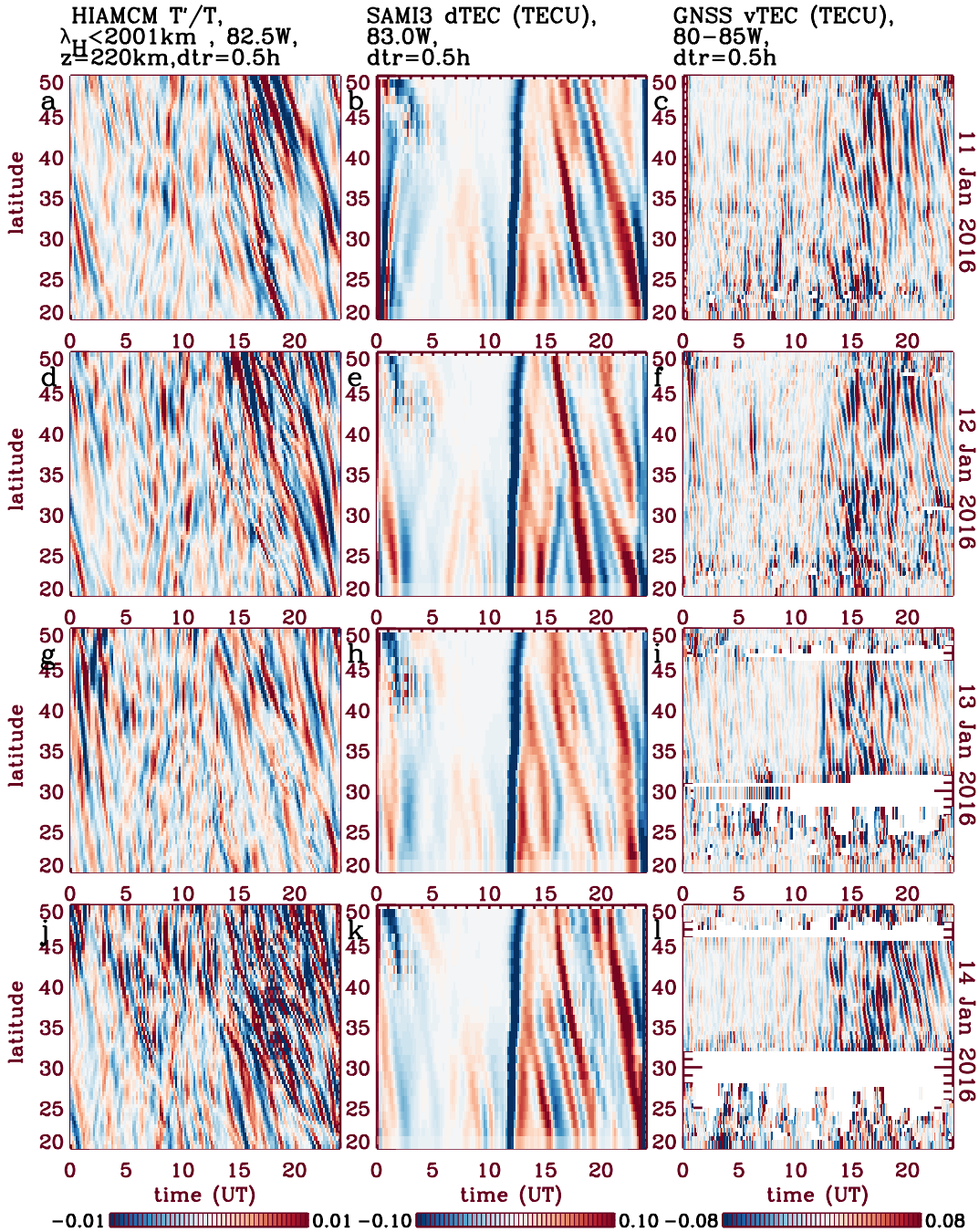

Figure 21. Same as Figure 18, except at 82.5°W (first column), at 83.0°W (second column), and averaged from 80–85°W (third column).

rings/arcs occur over Europe; for example, GWs propagate away from both (a) the UK and Poland at 10:35 UT on 11 January, (b) the UK and northern Norway at 12:05 UT on 11 January, and (c) the UK and southern Sweden at 9:20 UT on 12 January. During the daytime, the MSTIDs mainly propagate southeast/south/southwestward over Europe.

In addition, Movie S2 shows that MSTIDs propagate southeast/south/southwestward over the CONUS at ~18 UT until ~3 UT on the following day. These are mainly daytime TIDs. Over the course of each day, the MSTID propagation direction rotates clockwise in time from southeastward to southward then to southwestward.

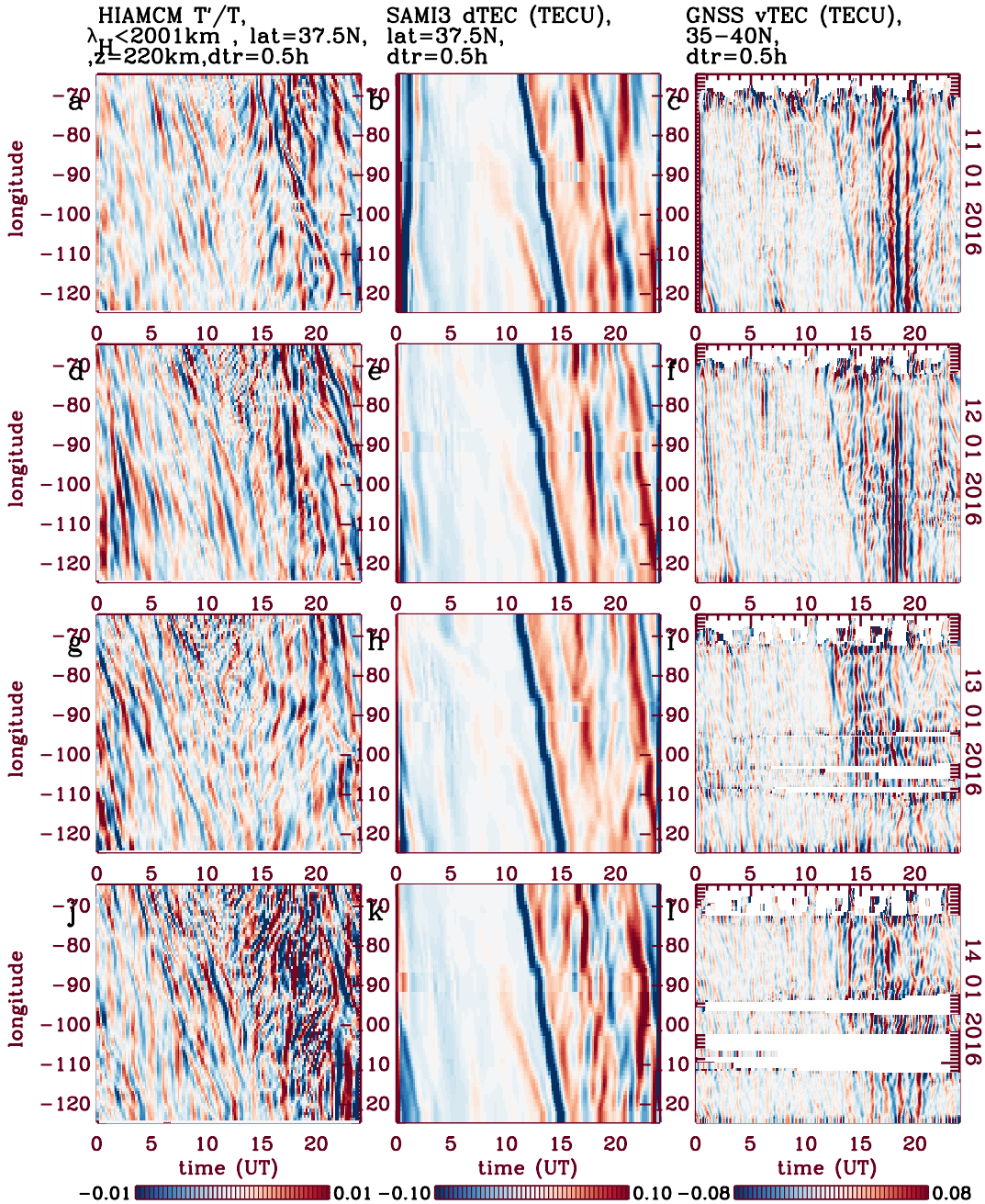

Figure 22. Same as Figure 19, except at 37.5°N (first and second columns), and averaged from 35–40°N (third column).

Occasionally, the MSTIDs have partial arc-like structure over the CONUS. For example, one such structure occurs over the eastern CONUS at 15:05 UT on 11 January. These MSTIDs propagate southeast/south/southwestward, with an approximate ring center over southern/central Canada at (95°W, 52°N). At this time, most of the minor core of the stratospheric polar vortex jet is located over Canada and the northeastern United States, with a strong southeastward flow speed of ∼100−130 m/s at $z = 40$ km at the ring center location (V24). Another example occurs at 23:30 UT on 12 January. These MSTIDs propagate south/southwestward, with an approximate ring center over the northeastern United States at (75°W, 42°N). At this time, the minor core of the polar vortex jet is in a similar location as in the previous example (i.e., at 15:05 UT on 11 January), with a southeastward flow speed of ∼75 m/s at $z = 40$ km at the ring center location (V24).

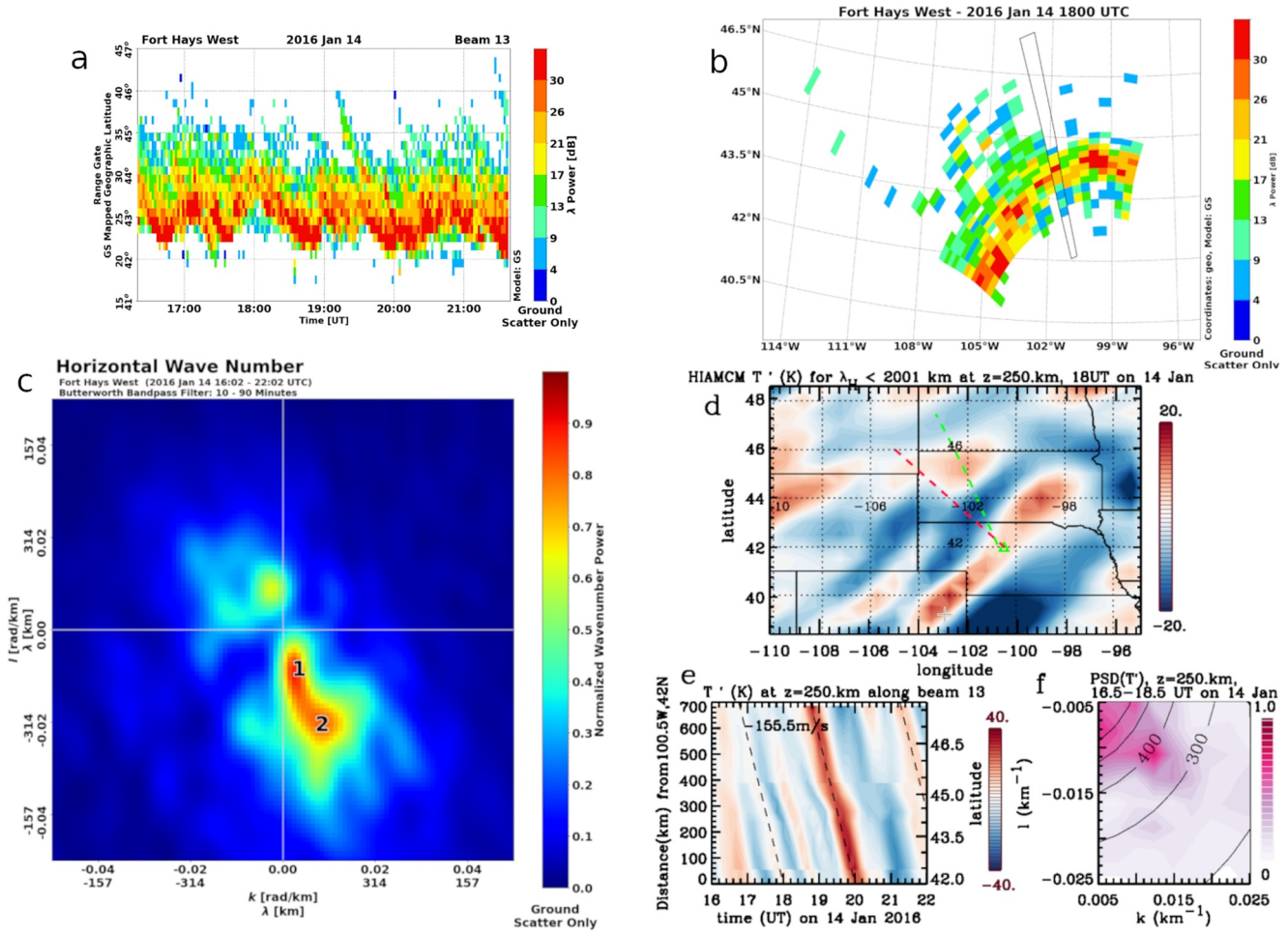

Figure 23. (a)–(c): Analysis of TIDs observed by the SuperDARN radar at Fort Hays West (FHW) on 14 January 2016 over the US. (a) λ power (in dB) from 16:02 to 22:02 UTC at 41–47°N along beam 13. (b) Map of λ power spectrum (in dB) for a two-minute scan starting at 18:00 UTC. The black outline shows beam 13. (c) Normalized average horizontal wave number spectrum from 16:02 to 22:02 UTC as functions of the zonal (k) and meridional (l) wavenumbers (in rad/km). (d)–(f): Analysis of the HIAMCM T' (in K) at $z = 250$ km on 14 January 2016 for GWs with $\lambda_H < 2001$ km. (d) Map of T' at 18:00 UT over the US. The green dash line shows beam 13, and the green triangle shows 100.5°W and 42°N. The red dash line shows the approximate propagation direction of the GWs at 100.5°W and 42°N. (e): Keogram of T' as a function of distance (in km) from 100.5°W and 42°N along beam 13. The dashed lines show −155.5 m/s. (f) Power spectrum of T' averaged over 16.5–18.5 UT at 110–95°W and 38.5–48.5°N as functions of k and l. Solid contours show $\lambda_H = 2\pi/\sqrt{k^2 + l^2}$ from 200 to 600 km in intervals of 100 km.

6.4. SuperDARN Observations of TIDs

SuperDARN (Greenwald et al., 1995) observations have been used to investigate TIDs generated by GWs (e.g., Bristow et al., 1994; Frissell et al., 2014, 2016; Samson et al., 1990). Here we present data from the SuperDARN radar at Fort Hays West, Kansas (FHW) over the United States on 14 January 2016 from 16:02–22:02 UTC. This time period and radar were chosen because they are representative of the daytime TID activity observed by North American SuperDARN radars during periods of high GW activity during the polar vortex jet event being investigated in this paper. We follow the formalism discussed by Frissell et al. (2014, 2016) for our analysis here.

Figure 23a shows the SuperDARN ground scatter λ power parameter from 16:02–22:02 UTC at 41–47°N along beam 13 of the radar. Here, the data is mapped to the ionospheric refraction point using the Ground Scatter mapping model. FHW beam 13 is indicated by a black outline in the map of the λ power spectrum shown in Figure 23b. The ground scatter λ power represents the strength of radar echoes from the ground after being refracted through the ionosphere. A ground scatter mapping (Bristow et al., 1994; Frissell et al., 2014) is used to plot the radar returns at their approximate ionospheric refraction point. TIDs passing through the radar field-of-view (FOV) cause the radar rays to focus and defocus, manifesting as perturbations of the λ power. In Figure 23a, the TIDs appear as quasi-periodic bright red features with negative slopes, indicating the TID is moving toward

the radar (southward). Figure 23b provides spatial context by showing a single two-minute scan of the FHW λ power beginning at 18:00 UTC. The TID wavefront can be seen as the red λ power enhancement in the middle of the FOV. A MUltiple SIgnal Classification (MUSIC) analysis using the techniques described by Frissell et al. (2014) was applied to the radar data for the six-hour period from 16:02–22:02 UTC. The data was filtered with a 10–90 min Butterworth bandpass filter to select for oscillations in the MSTID band. Figure 23c shows the wavenumber spectrum result of this analysis. The TIDs at 95−110°W and 38.5−48.5°N propagated predominantly southward with horizontal wavelengths of $\lambda_H \sim 615$ km (marked "1") to $\lambda_H \sim 300$ km (marked "2"). Using a Fast Fourier Transform (FFT) analysis, it was determined that the dominant TID period observed during this time period was $\tau_r \sim 45$ min.

Figure 23d shows a horizontal map of the HIAMCM T' at 18:00 UT and $z = 250$ km on 14 January 2016 for GWs with $\lambda_H < 2001$ km. Medium-scale GWs are observed in the FHW FOV of beam 13. Note that the approximate GW propagation direction (red dash line) is nearly parallel to beam 13 (green dash line). Figure 23e shows a keogram of T' as a function of distance from 100.5°W and 42°N along beam 13. The GWs propagate southeastward with $\tau_r \sim 40 - 50$ min at ~18 UT, in good agreement with the SuperDARN data. The distance between the phase fronts (along beam 13) at 18 UT is ~400 km. These GWs have phase speeds (along beam 13) of −155.5 m/s from 16 to 22 UT (dashed lines). Since the azimuth of beam 13 is $\theta_{13} = -25.3°$ and that of the GWs is $\theta_{GW} = -48.4°$ (red dash line in Figure 23d), we estimate that the GW's horizontal phase speed is $c_H \sim -155.6 \times \cos(|\theta_{13} - \theta_{GW}|) \sim 143$ m/s and that the GW's horizontal wavelength is $\lambda_H \sim 400 \times \cos(|\theta_{13} - \theta_{GW}|) \sim 370$ km. Figure 23f shows the average power spectrum of T' from 16.5 to 18.5 UT as functions of k and l. Here we only average over 16.5–18.5 UT to avoid the large-scale GWs dominant at 19–22 UT. The peak horizontal wavelengths of the medium-scale GWs are $\lambda_H \sim 350 - 700$ km, in good agreement with the SuperDARN data. Thus τ_r, λ_H and the propagation directions of the simulated medium-scale GWs agree well with that of the MSTIDs observed by SuperDARN FHW.

7. Conclusions

In this paper, we simulated the GWs and TIDs during 11–15 January 2016 using the HIAMCM-SAMI3. No geomagnetic forcing was included. We found that MSTIDs and large-scale TIDs (LSTIDs) are generated by medium and large-scale higher-order GWs "from" (i.e., generated/magnified by) the entrance, core and exit regions of the polar vortex jet. We found that these higher-order GWs were concentrated at the highest latitudes of 60 − 90°N at $z \geq 200$ km, in agreement with GOCE and CHAMP satellite data. The model results showed that (a) many of the TIDs over Europe have concentric ring/arc-like structure, and (b) most of the TIDs over North/South America occurred during the daytime, propagated southward from high latitudes, and had planar wave structure. The reason the TIDs have concentric ring/arc-like structure over Europe is because they are generated by higher-order GWs created from LBFs over Europe; it is well-known that LBFs generate GWs with concentric ring-like structures (Vadas et al., 2003, 2018). The reason the TIDs have planar structure over North/South America is because they propagated large distances from their sources and because only a small angular portion of the ring is seen at that distance. The latter TIDs were found to arise from higher-order GWs which propagated over the Arctic region and southward over North America. Because these latter cross-polar TIDs arose from high latitudes and propagated southward over North America during the daytime, such TIDs could be misidentified as arising from geomagnetic forcing. (Note that GWs are also generated by geomagnetic forcing (e.g., Hocke & Schlegel, 1996)). We found that some of the LSTIDs from the core of the polar vortex jet over Europe crossed into the southern hemisphere to ~30°S. Therefore, the polar vortex jet facilitates the generation of TIDs worldwide via higher-order GWs from MSVC. We also found that some of the higher-order GWs/TIDs from the major core of the polar vortex jet (over Europe) propagated to equatorial latitudes, and were present when EPBs formed there. We also note that Bossert et al. (2024) found that increased EPB activity over South America coincided with northward quasi-two day wave phase in the southern hemisphere, and increased GW activity and temperature variation in the northern hemisphere linked to the polar vortex.

We also compared the simulated GWs and TIDs with observations. We found upward and downward TIDs in the D and E regions with fishbone structures in $z - t$ plots in EISCAT (in manda mode) observations at Tromsø, Norway. Here, the TIDs with upward and downward phase lines had similar τ and λ_z, which is an indicator for the presence of secondary GWs. Upon comparing with the HIAMCM GWs, we found good agreement between τ, λ_z and the "knee" altitudes of the simulated GWs and observed TIDs at $z \sim 70-90$ km. We found that the periods τ

and vertical wavelengths λ_z of the modeled GWs in the F region agreed well with that of the TIDs observed by EISCAT (in bella mode) at Tromsø, Norway on 11–12 January. Good agreement was found between the simulated southward-propagating GWs over Alaska and those observed by PFISR on 14–15 January. We found that the modeled GWs and TIDs agreed well with the dTEC observed by GNSS over Europe and North America via horizontal maps and keograms. We found that the horizontal wavelengths, periods and propagation directions of the simulated medium-scale GWs agreed with the MSTIDs observed by the FHW SuperDARN over the CONUS on 14 January. We also compared the simulated EPBs over Brazil with those observed by GNSS, and found reasonably good agreement on 13 and 14 January.

Because of the generally-good agreement between the simulated and observed GWs and TIDs, we conclude that multi-step vertical coupling (MSVC) of GWs generated/amplified by the polar vortex jet is an important source of GWs and TIDs in the thermosphere and ionosphere. Via this mechanism, momentum and energy from GWs generated by sources in the lower/middle atmosphere are transferred into higher-order GWs and TIDs in the thermosphere and F region.

Appendix A: Traveling Atmospheric Disturbances

A1. TADs Observed by GOCE and CHAMP

The Gravity Field and Ocean Circulation Explorer (GOCE) satellite orbited Earth from 2009 to 2013 at $z \sim 250{-}290$ km (Doornbos, 2019), and The Challenging Minisatellite Payload (CHAMP) satellite orbited Earth from 2000 to 2009 at $z \sim 450$ to 260 km (Reigber et al., 2002). These data were used to study TADs (e.g., Bruinsma & Forbes, 2008; Park et al., 2014; Trinh et al., 2018; Xu et al., 2021). Although TADs include GWs, TADs also include localized, non-propagating wind and density changes that result from momentum deposition (Vadas et al., 2003). The GW polarization and dispersion relations are needed to identify which TADs are GWs (Vadas & Nicolls, 2012; Vadas et al., 2019; Xu et al., 2024). Although GOCE and CHAMP did not sample the thermosphere during our case study, we display the quiet-time winter TAD distributions here to gain additional insight into our simulation results. The TADs are extracted using a Butterworth Fourier transform filter as described in Xu et al. (2021). The TADs are averaged over 2009–2013 (GOCE) and 2004–2007 (CHAMP). The average satellite altitudes during these times are $z \sim 266$ km (GOCE) and $z \sim 364$ km (CHAMP). The GOCE data contains local solar times (LST) of ~6–7 LST and ~18−19 LST, while the CHAMP data covers all LSTs.

Figure A1 shows $\overline{(100\rho'/\overline{\rho})^2}$ for quiet-time TADs with along-track wavelengths of $160 < \lambda_{\text{track}} < 2001$ km for Kp = [0, 3] during December-January from GOCE (a, c) and CHAMP (b, d). Note that both data sets (especially GOCE) show TAD enhancements in the North American/Greenland sector. As discussed below, these enhancements likely arise from geomagnetic activity. However, both also show a somewhat smaller-amplitude uniform distribution in geographic longitude that are poleward of 75°N, as well as a weaker-amplitude uniform distribution in geographic longitude at 55–75°N (dash turquoise lines show geographic latitudes of 55°N and 75°N). The uniformly-distributed CHAMP TADs have average amplitudes of $|100\rho'/\overline{\rho}| \sim 2{-}4\%$ at 60−85°N and ~1−2% at 40−60°N.

Comparing the "longitudinally-uniform" portion of Figure A1 with the simulation results shown in Figures 4d–4e and 4i–4j, many similarities exist, including that the simulated GWs and observed TADs are spread out fairly uniformly in longitude, are concentrated at high latitudes of 60−90°N, and have similar amplitudes. Thus, it is likely that many of the quiet-time, wintertime TADs observed by GOCE and CHAMP are higher-order GWs. This conclusion is supported by recent work of Xu et al. (2024), who extracted the GWs from GOCE and CHAMP data using the GW polarization and dispersion relations. They found that quiet-time GOCE and CHAMP wintertime GWs are concentrated at high latitudes and are spread out fairly evenly in longitude, although with an additional enhancement in the North American/Greenland sector (their Figs. 7–10). These GWs had $\lambda_H \sim 400{-}1000$ km, intrinsic horizontal phase speeds of $c_{IH} = 600 - 800$ m/s, and intrinsic periods of $\tau_{Ir} = 10{-}20$ min. These GWs must have originated in the thermosphere, since (a) a GW cannot have c_{IH} larger than the local sound speed (Vadas & Crowley, 2010; Vadas et al., 2019), which is $c_s \sim 280{-}310$ m/s at $z < 100$ km, and (b) c_H is roughly constant along a GW's ray path if the background atmosphere changes relatively slowly in time and horizontal wind shears are small (Eqs. 7–8 from Vadas & Becker, 2018).

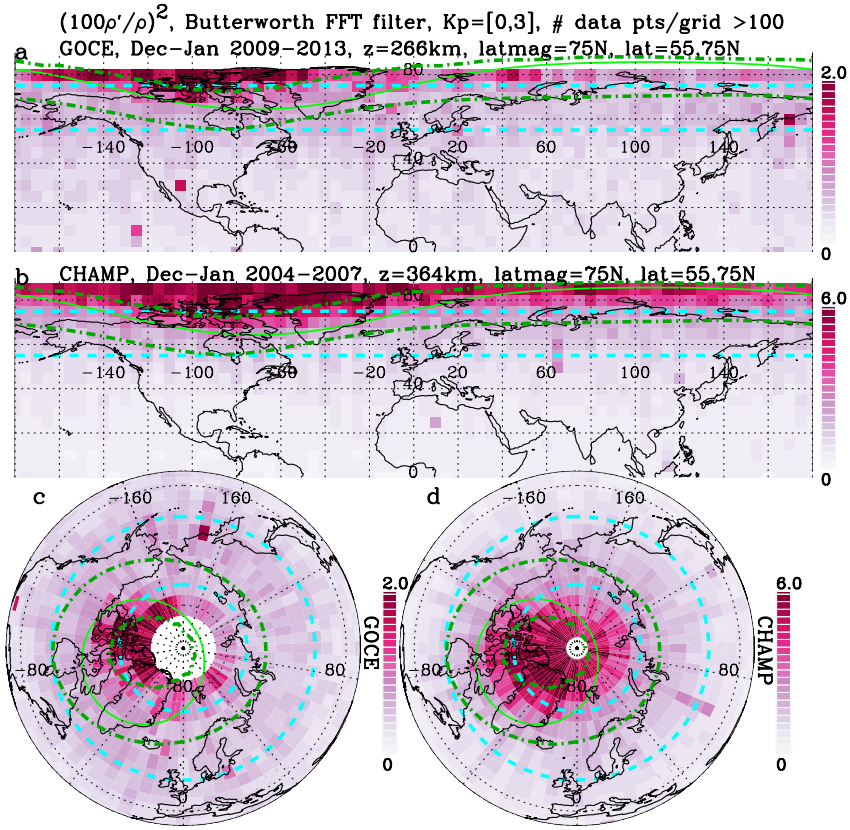

Figure A1. The average density perturbations squared, $\overline{(100\rho'/\overline{\rho})^2}$ (colors), for quiet-time TADs with along-track horizontal wavelengths $160 < \lambda_{track} < 2001$ km for $0 \leq$ Kp ≤ 3. The TADs are extracted using a Butterworth FFT filter. Bins are displayed with ≥100 data points. (a) TADs from the GOCE averaged during December–January 2009–2013. The average altitude during this time is $z \sim 266$ km. The green solid line shows magnetic latitude 75°N, while the dash turquoise lines show geographic latitudes 55°N and 75°N. The dark green dash-dot lines show an average auroral occurrence rate of 50% during December-January in 2009–2013. Panel (b): same as (a), but for CHAMP averaged during December–January 2004–2007. The average altitude during this time is $z \sim 364$ km. The dark green dash-dot lines are the same as in panel (a) except in 2004–2007. Panels (c) and (d): same as (a) and (b) but for polar projections. The colors are oversaturated to see the GWs.

A2. Contribution to the Observed TADs From Auroral Activity

To assess the location of the auroral oval for the GOCE and CHAMP maps shown in Figure A1, we run the Empirical Canadian High Arctic Ionospheric Model (E-CHAIM) for December through January during 2004–2007 and 2009–2013 (Themens et al., 2020; Watson et al., 2021). For each timestep, the aurora is flagged as present when the modeled auroral precipitation flux is greater than 0.25 erg/cm^2/s, consistent with the Zhang and Paxton (2008) model used to identify the auroral boundaries in the International Reference Ionosphere (IRI) model (Bilitza et al., 2022). Flagged auroral presence is binned in latitude/longitude and an occurrence rate/probability of auroral precipitation is generated. To illustrate the average location of the auroral oval, we overplot boundaries where the occurrence rate exceeds 50% during December-January in 2009–2013 (a, c) and 2004–2007 (b, d) in Figure A1 (dark green dash-dot lines). The distributions extend asymmetrically into the North American/Greenland sector. Thus the TAD amplitude enhancements there in Figure A1 are likely caused by geomagnetic activity.

Data Availability Statement

MERRA-2 reanalysis data (Bosilovich et al., 2015) is available at the Data and Information Services Center, managed by the NASA Goddard Earth Sciences (GES) at https://goldsmr5.gesdisc.eosdis.nasa.gov/data/MERRA2/M2I6NVANA.5.12.4/. GOCE v1.5 data and CHAMP data access is: http://thermosphere.tudelft.nl/.

AIRS variance data is available for download at https://datapub.fz-juelich.de/slcs/airs/gravity_waves/data/variance_4mu/. All ISR data are publicly available from both the SRI and Madrigal databases: https://amisr.com/amisr/links/data-access/. EISCAT is an international association supported by research organizations in China (CRIRP), Finland (SA), Japan (NIPR and ISEE), Norway (NFR), Sweden (VR), and the United Kingdom (UKRI). EISCAT data can be downloaded at https://madrigal.eiscat.se/madrigal. The GNSS receiver data from the Madrigal database is available for download at http://cedar.openmadrigal.org/. CDDOS GNSS data is available at https://cddis.nasa.gov/archive/gnss/products/. FINPOS GNSS data is available at https://www.maanmittauslaitos.fi/en/finpos/rinex. The Quebec Geodetic Service data is available at https://mrnf.gouv.qc.ca/repertoire-geographique/reseau-geodesique-donnees-gnss/. The NERC British Isles continuous GNSS Facility data is available at https://www.bigf.ac.uk/. Maps of INPE's GNSS data are available at https://www2.inpe.br/climaespacial/portal/tec-map-daily-video/. FITACF (fit autocorrelation function) SuperDARN data (Shi et al., 2022) is available at https://superdarn.ca/data-download and can be analyzed and visualized with the PyDARN toolkit available from https://github.com/SuperDARN/ (Shi et al., 2022). SuperDARN MUSIC analysis was conducted with the PyDARNMusic library at https://github.com/hamSCI/pydarnmusic. The model data shown in this paper will be available at the time of publication at https://www.cora.nwra.com/vadas/Vadas-etal-JGR-2024-polarvortex-ionosphere-files/.

Acknowledgments

SLV was supported by NSF Grant AGS-1832988. SLV and EB were supported by NSF Grant 2329957, by NASA Grants 80NSSC20K0628, 80NSSC19K0836, 80NSSC22K0174, and 80NSSC24K0274, and by ONR Grant N00014-24-1-2367. DRT's and SJM's contribution to this study was supported by Natural Environment Research Council EISCAT3D DRIIVE Grant NE/W003368/1 and Office of Naval Research PRISM programme project N00014-23-S-B001. JDH was supported by NASA Grant 80NSSC22K0174. LG was supported by NASA Grant 80NSSC22K1074, AFOSR Grant FA9550-23-1-0474, and ONR Grant N00014-24-1-2122. KB was supported by AFOSR Grant FA9550-21-1-0189, and NASA Grants 80NSSC21K0002 and 80NSSC24K0274. CF was supported by Fundação de Apoio à Pesquisa do Estado da Paraíba (FAPESq) n° 2417/2023 and Conselho Nacional de Desenvolvimento Científico e Tecnológico (CNPq) n° 303871/2023-7. CF thanks INPE's space weather division for the GNSS data in Brazil used in Figures 10f and 10h. SX was supported by NSF Grant AGS-1832988 and NASA Grant 80NSSC19K0836. NAF, MJM, and TJP were supported by NSF Grant AGS-2045755 and NASA Grant 80NSSC23K0848/1564031. The Fort Hays West SuperDARN radar is maintained and operated by Virginia Tech with support from NSF under award AGS-1935110. We acknowledge the use of SuperDARN data. SuperDARN is a network of radars funded by national scientific funding agencies of Australia, Canada, China, France, Italy, Japan, Norway, South Africa, the United Kingdom, and the United States of America.

References

Alexander, M. J., & Teitelbaum, H. (2007). Observation and analysis of a large amplitude mountain wave event over the Antarctic Peninsula. *Journal of Geophysical Research*, *112*(D21), 103. https://doi.org/10.1029/2006JD008368

Andrews, D. G., Holton, J. R., & Leovy, C. B. (1987). Middle atmosphere dynamics. *International Geophysics Series*, *40*.

Azeem, I., Yue, J., Hoffmann, L., Miller, S. D., III, W. C. S., & Crowley, G. (2015). Multisensor profiling of a concentric gravity wave event propagating from the troposphere to the ionosphere. *Geophysical Research Letters*, *42*(19), 7874–7880. https://doi.org/10.1002/2015GL065903

Becker, E., Goncharenko, L., Harvey, V. L., & Vadas, S. L. (2022). Multi-step vertical coupling during the January 2017 sudden stratospheric warming. *Journal of Geophysical Research: Space Physics*, *127*(12), e2022JA030866. https://doi.org/10.1029/2022JA030866

Becker, E., & Vadas, S. L. (2020). Explicit global simulation of gravity waves in the thermosphere. *Journal of Geophysical Research: Space Physics*, *125*(10), e2020JA028034. https://doi.org/10.1029/2020JA028034

Becker, E., Vadas, S. L., Bossert, K., Harvey, V. L., Zülicke, C., & Hoffmann, L. (2022). A high-resolution whole-atmosphere model with resolved gravity waves and specified large-scale dynamics in the troposphere and stratosphere. *Journal of Geophysical Research: Space Physics*, *127*(2), e2021JD035018. https://doi.org/10.1029/2021JD035018

Bilitza, D., Pezzopane, M., Truhlik, V., Altadill, D., Reinisch, B. W., & Pignalberi, A. (2022). The international reference ionosphere model: A review and description of an ionospheric benchmark. *Reviews of Geophysics*, *60*(4), e2022RG000792. https://doi.org/10.1029/2022RG000792

Bosilovich, M. G., Akella, S., Coy, L., Cullather, R., Draper, C., Gelaro, R., et al. (2015). MERRA-2: Initial evaluation of the climate. *NASA Tech. Rep. Series on Global Modeling and Data Assimilation, NASA/TM-2015-104606/Vol. 43, Goddard Space Flight Center*.

Bossert, K., Kumari, K., Inchin, P., Norrell, J., Eckermann, S., Pautet, P.-D., et al. (2024). Influences of the quasi-two-day wave on plasma bubble behavior over South America. *Frontiers in Astronomy and Space Sciences*, *11*. https://doi.org/10.3389/fspas.2024.1465230

Bristow, W. A., Greenwald, R. A., & Samson, J. C. (1994). Identification of high-latitude acoustic gravity wave sources using the Goose Bay HF radar. *Journal of Geophysical Research*, *99*(A1), 319–331. https://doi.org/10.1029/93ja01470

Bruinsma, S., & Forbes, J. (2008). Medium to large-scale density variability as observed by CHAMP. *Space Weather*, *6*, S08002. https://doi.org/10.1029/2008SW000411

Djuth, F. T., Sulzer, M. P., Gonzáles, S. A., Mathews, J. D., Elder, J. H., & Walterscheid, R. L. (2004). A continuum of gravity waves in the Arecibo thermosphere? *Geophysical Research Letters*, *31*(16), L16801. https://doi.org/10.1029/2003GL019376

Doornbos, E. (2019). *Air density and wind retrieval using GOCE data, Ao/1-6367/10/nl/af, version 2.0 data set user manual*. European Space Agency (ESA). Retrieved from https://earth.esa.int/eogateway/documents/20142/37627/GOCE-thermospheric-dataset-user-manual.pdf

Emmert, J. T., Drob, D. P., Picone, J. M., Siskind, D. E., Jones, M., Jr., Mlynczak, M. G., et al. (2021). NRLMSIS 2.0: A whole-atmosphere empirical model of temperature and neutral species densities. *Earth and Space Science*, *8*(3), e2020EA001321. https://doi.org/10.1029/2020EA001321

England, S. L., Greer, K. R., Zhang, S.-R., Evans, S., Solomon, S. C., Eastes, R. W., et al. (2021). First comparison of traveling atmospheric disturbances observed in the middle thermosphere by Global-scale Observations of the Limb and Disk to traveling ionospheric disturbances seen in ground-based total electron content observations. *Journal of Geophysical Research: Space Physics*, *126*(6), e2021JA029248. https://doi.org/10.1029/2021JA029248

Forbes, J. M., Bruinsma, S. L., Miyoshi, Y., & Fujiwara, H. (2008). A solar terminator wave in thermosphere neutral densities measured by the CHAMP satellite. *Geophysical Research Letters*, *35*(14), L14802. https://doi.org/10.1029/2008GL034075

Frissell, N. A., Baker, J., Ruohoniemi, J. M., Gerrard, A. J., Miller, E. S., Marini, J. P., et al. (2014). Climatology of medium-scale traveling ionospheric disturbances observed by the midlatitude Blackstone SuperDARN radar. *Journal of Geophysical Research: Space Physics*, *119*(9), 7679–7697. https://doi.org/10.1002/2014JA019870

Frissell, N. A., Baker, J. B. H., Ruohoniemi, J. M., Greenwald, R. A., Gerrard, A. J., Miller, E. S., & West, M. L. (2016). Sources and characteristics of medium-scale traveling ionospheric disturbances observed by high-frequency radars in the North American sector. *Journal of Geophysical Research: Space Physics*, *121*(4), 3722–3739. https://doi.org/10.1002/2015JA022168

Gasque, L. C., Harding, B. J., Immel, T. J., Wu, Y.-J., Triplett, C. C., Vadas, S. L., et al. (2024). Evening solar terminator waves in Earth's thermosphere: Neutral wind signatures observed by ICON-MIGHTI. *Journal of Geophysical Research: Space Physics*, *129*(2), e2023JA032274. https://doi.org/10.1029/2023JA032274

Greenwald, R. A., Baker, K. A., Dudeney, J. R., Pinnock, M., Jones, T. B., Thomas, E. C., et al. (1995). DARN/SuperDARN: A global view of the dynamics of high-latitude convection. *Space Science Reviews*, *71*(1–4), 761–796. https://doi.org/10.1007/BF00751350

Harvey, V. L., Pierce, R. B., Fairlie, T. D., & Hitchman, M. H. (2002). A climatology of stratospheric polar vortices and anticyclones. *Journal of Geophysical Research*, *107*(D20), ACL10-1–ACL10-22. https://doi.org/10.1029/2001JD001471

Harvey, V. L., Randall, C. E., Goncharenko, L. P., Becker, E., Forbes, J. M., Carstens, J., et al. (2023). CIPS observations of gravity wave activity at the edge of the polar vortices and coupling to the ionosphere. *Journal of Geophysical Research: Atmospheres*, *128*(12), e2023JD038827. https://doi.org/10.1029/2023JD038827

Heale, C. J., Inchin, P. A., & Snively, J. B. (2022). Primary versus secondary gravity wave responses at F-region heights generated by a convective source. *Journal of Geophysical Research: Space Physics*, *127*(1), e2021JA029947. https://doi.org/10.1029/2021JA029947

Hedin, A., & Mayr, H. (1987). Characteristics of wavelike fluctuations in Dynamics Explorer neutral composition data. *Journal of Geophysical Research*, *92*(A10), 11159–11172. https://doi.org/10.1029/ja092ia10p11159

Hocke, K., & Schlegel, K. (1996). A review of atmospheric gravity waves and travelling ionospheric disturbances: 1982-1995. *Annals of Geophysics*, *14*(9), 917–940. https://doi.org/10.1007/s00585-996-0917-6

Hoffmann, L., Alexander, M. J., Clerbaux, C., Grimsdell, A. W., Meyer, C. I., Robler, T., & Tournier, B. (2014). Intercomparison of stratospheric gravity wave observations with AIRS and IASI. *Atmospheric Measurement Techniques*, *7*(12), 4517–4537. https://doi.org/10.5194/amt-7-4517-2014

Hoffmann, L., Xue, X., & Alexander, M. J. (2013). A global view of stratospheric gravity wave hotspots located with Atmospheric Infrared Sounder observations [Dataset]. *Journal of Geophysical Research: Atmospheres*, *118*(2), 416–434. https://doi.org/10.1029/2012JD018658

Huba, J., Joyce, G., & Fedder, J. (2000). SAMI2 (Sami2 is another model of the ionosphere): A new low-latitude ionosphere model. *Journal of Geophysical Research*, *105*(A10), 23035–23053. https://doi.org/10.1029/2000JA000035

Huba, J. D., Becker, E., & Vadas, S. L. (2023). Simulation study of the 15 January 2022 Tonga event: Development of super equatorial plasma bubbles. *Geophysical Research Letters*, *50*(1), e2022GL101185. https://doi.org/10.1029/2022GL101185

Liu, H., Pedatella, N., & Hocke, K. (2017). Medium-scale gravity-wave activity in the bottomside F region in tropical regions. *Geophysical Research Letters*, *44*(14), 7099–7105. https://doi.org/10.1002/2017GL073855

Lund, T. S., & Fritts, D. C. (2012). Numerical simulation of gravity wave breaking in the lower thermosphere. *Journal of Geophysical Research*, *117*, D21105. https://doi.org/10.1029/2012JD017536

Matthias, V., Dörnbrack, A., & Stober, G. (2016). The extraordinarily strong and cold polar vortex in the early northern winter 2015/2016. *Geophysical Research Letters*, *43*(12), 12287–12294. https://doi.org/10.1002/2016GL071676

Matzka, J., Stolle, C., Yamazaki, Y., Bronkalla, O., & Morschhauser, A. (2021). The geomagnetic Kp index and derived indices of geomagnetic activity. *Space Weather*, *19*(5), e2020SW002641. https://doi.org/10.1029/2020SW002641

Mrak, S., Semeter, J., Nishimura, Y., & Coster, A. J. (2021). Extreme low-latitude total electron content enhancement and global positioning system scintillation at dawn. *Space Weather*, *19*(9), e2021SW002740. https://doi.org/10.1029/2021SW002740

Nicolls, M. J., & Heinselman, C. J. (2007). Three-dimensional measurements of traveling ionospheric disturbances with the Poker Flat Incoherent Scatter Radar. *Geophysical Research Letters*, *34*(21), L21104. https://doi.org/10.1029/2007GL031506

Nicolls, M. J., Vadas, S. L., Aponte, N., & Sulzer, M. P. (2014). Horizontal wave parameters of daytime thermospheric gravity waves and E-region neutral winds over Puerto Rico. *Journal of Geophysical Research*, *119*, 576–600. https://doi.org/10.1002/2013JA018988

Nishioka, M., Tsugawa, T., Kubota, M., & Ishii, M. (2013). Concentric waves and short-period oscillations observed in the ionosphere after the 2013 Moore EF5 tornado. *Geophysical Research Letters*, *40*(21), 5581–5586. https://doi.org/10.1002/2013GL057963

O'Sullivan, D., & Dunkerton, T. J. (1995). Generation of inertia-gravity waves in a simulated life-cycle of baroclinic instability. *Journal of the Atmospheric Sciences*, *52*(21), 3695–3716. https://doi.org/10.1175/1520-0469(1995)052<3695:goiwia>2.0.co;2

Otsuka, Y., Ogawa, T., Saito, A., Tsugawa, T., Fukao, S., & Miyazaki, S. (2002). A new technique for mapping of total electron content using GPS network in Japan. *Earth Planets and Space*, *54*(1), 63–70. https://doi.org/10.1186/BF03352422

Ozeki, M., & Heki, K. (2010). Ionospheric holes made by ballistic missiles from North Korea detected with a Japanese dense GPS array. *Journal of Geophysical Research*, *115*(A9), A09314. https://doi.org/10.1029/2010JA015531

Park, J., Lühr, H., Lee, C., Kim, Y. H., Jee, G., & Kim, J.-H. (2014). A climatology of medium-scale gravity wave activity in the midlatitude/low-latitude daytime upper thermosphere as observed by CHAMP. *Journal of Geophysical Research: Space Physics*, *119*(3), 2187–2196. https://doi.org/10.1002/2013JA019705

Plougonven, R., & Zhang, F. (2014). Internal gravity waves from atmospheric jets and fronts. *Reviews of Geophysics*, *52*(1), 33–76. https://doi.org/10.1002/2012RG000419

Reigber, C., Lühr, H., & Schwintzer, P. (2002). CHAMP mission status. *Advances in Space Research*, *30*(2), 129–134. https://doi.org/10.1016/s0273-1177(02)00276-4

Samson, J. C., Greenwald, R. A., Ruohoniemi, J. M., Frey, A., & Baker, K. B. (1990). Goose Bay radar observations of Earth-reflected, atmospheric gravity waves in the high-latitude ionosphere. *Journal of Geophysical Research*, *95*(A6), 7693–7709. https://doi.org/10.1029/JA095iA06p07693

Shi, X., Schmidt, M., Martin, C. J., Billett, D. D., Bland, E., Tholley, F. H., et al. (2022). pyDARN: A Python software for visualizing SuperDARN radar data. *Frontiers in Astronomy and Space Sciences*, *9*. https://doi.org/10.3389/fspas.2022.1022690

Stober, G., Matthias, V., Jacobi, C., Wilhelm, S., Höffner, J., & Chau, J. L. (2017). Exceptionally strong summer-like zonal wind reversal in the upper mesosphere during winter 2015/16. *Annales Geophysicae*, *35*(3), 711–720. https://doi.org/10.5194/angeo-35-711-2017

Takahashi, H., Costa, S., Otsuka, Y., Shiokawa, K., Monico, J., Paula, E., et al. (2014). Diagnostics of equatorial and low latitude ionosphere by TEC mapping over Brazil. *Advances in Space Research*, *54*(3), 385–394. https://doi.org/10.1016/j.asr.2014.01.032

Takahashi, H., Wrasse, C., Otsuka, Y., Ivo, A., Gomes, V., Paulino, I., et al. (2015). Plasma bubble monitoring by TEC map and 630nm airglow image. *Journal of Atmospheric and Solar-Terrestrial Physics*, *130–131*, 151–158. https://doi.org/10.1016/j.jastp.2015.06.003

Takahashi, H., Wrasse, C. M., Denardini, C. M., Pádua, M. B., de Paula, E. R., Costa, S. M. A., et al. (2016). Ionospheric TEC weather map over South America. *Space Weather*, *14*(11), 937–949. https://doi.org/10.1002/2016SW001474

Themens, D. R., Watson, C., McCaffrey, A., Reid, B., & Jayachandran, P. (2020). The development and implementation of a precipitation enhanced E-region for E-CHAIM, report submitted to defence research and development Canada for contract #W7714-186507/001/SS. Retrieved from https://cradpdf.drdc-rddc.gc.ca/PDFS/unc370/p813718_A1b.pdf

Themens, D. R., Watson, C., Žagar, N., Vasylkevych, S., Elvidge, S., McCaffrey, A., et al. (2022). Global propagation of ionospheric disturbances associated with the 2022 Tonga volcanic eruption. *Geophysical Research Letters*, *49*(7), e2022GL098158. https://doi.org/10.1029/2022GL098158

Trinh, Q. T., Ern, M., Doornbos, E., Preusse, P., & Riese, M. (2018). Satellite observations of middle atmosphere-thermosphere vertical coupling by gravity waves. *Annals of Geophysics*, *36*(2), 425–444. https://doi.org/10.5194/angeo-36-425-2018

Tsunoda, R. T. (2005). On the enigma of day-to-day variability in equatorial spread F. *Geophysical Research Letters*, *32*(8), L08103. https://doi.org/10.1029/2005GL022512

Tsunoda, R. T. (2010). On equatorial spread F: Establishing a seeding hypothesis. *Journal of Geophysical Research*, *115*(A12), A12303. https://doi.org/10.1029/2010JA015564

Vadas, S. L. (2007). Horizontal and vertical propagation and dissipation of gravity waves in the thermosphere from lower atmospheric and thermospheric sources. *Journal of Geophysical Research*, *112*(A6), A06305. https://doi.org/10.1029/2006JA011845

Vadas, S. L., & Azeem, I. (2021). Concentric secondary gravity waves in the thermosphere and ionosphere over the continental United States on 25-26 March 2015 from deep convection. *Journal of Geophysical Research: Space Physics*, *126*(2), e2020JA028275. https://doi.org/10.1029/2020JA028275

Vadas, S. L., & Becker, E. (2018). Numerical modeling of the excitation, propagation, and dissipation of primary and secondary gravity waves during wintertime at McMurdo Station in the Antarctic. *Journal of Geophysical Research: Atmospheres*, *123*(17), 9326–9369. https://doi.org/10.1029/2017JD027974

Vadas, S. L., & Becker, E. (2019). Numerical modeling of the generation of tertiary gravity waves in the mesosphere and thermosphere during strong mountain wave events over the Southern Andes. *Journal of Geophysical Research: Space Physics*, *124*(9), 7687–7718. https://doi.org/10.1029/2019JA026694

Vadas, S. L., Becker, E., Bossert, K., Baumgarten, G., Hoffmann, L., & Harvey, V. L. (2023). Secondary gravity waves from the stratospheric polar vortex over ALOMAR Observatory on 12-14 January. *Journal of Geophysical Research: Atmospheres*, *128*(2), e2022JD036985. https://doi.org/10.1029/2022JD036985

Vadas, S. L., Becker, E., Bossert, K., Hozumi, Y., Stober, G., Harvey, V. L., et al. (2024). The role of the polar vortex jet for secondary and higher-order gravity waves in the northern mesosphere and thermosphere during 11-14 january 2016. *Journal of Geophysical Research: Space Physics*, *129*(9), e2024JA032521. https://doi.org/10.1029/2024JA032521

Vadas, S. L., Becker, E., Figueiredo, C., Bossert, K., Harding, B., & Gasque, C. (2023). Primary and secondary gravity waves and global wind changes generated by the Tonga volcanic eruption on 15 January 2022: Modeling and comparison with ICON-MIGHTI winds. *Journal of Geophysical Research: Space Physics*, *128*(2), e2022JA031138. https://doi.org/10.1029/2022JA031138

Vadas, S. L., & Crowley, G. (2010). Sources of the traveling ionospheric disturbances observed by the ionospheric TIDDBIT sounder near Wallops Island on October 30, 2007. *Journal of Geophysical Research*, *115*(A7), A07324. https://doi.org/10.1029/2009JA015053

Vadas, S. L., Figueiredo, C., Becker, E., Huba, J. D., Themens, D. R., Hindley, N., et al. (2023). Traveling ionospheric disturbances induced by the secondary gravity waves from the Tonga eruption on 15 January 2022: Modeling with MESORAC-HIAMCM-SAMI3 and comparison with GPS/TEC and ionosonde data. *Journal of Geophysical Research: Space Physics*, *128*(6), e2023JA031408. https://doi.org/10.1029/2023JA031408

Vadas, S. L., Fritts, D. C., & Alexander, M. J. (2003). Mechanism for the generation of secondary waves in wave breaking regions. *Journal of the Atmospheric Sciences*, *60*(1), 194–214. Retrieved from https://journals.ametsoc.org/view/journals/atsc/60/1/1520-0469_2003_060_0194_mftgos_2.0.co_2.xml?tab_body=pdf

Vadas, S. L., & Nicolls, M. J. (2008). Using PFISR measurements and gravity wave dissipative theory to determine the neutral, background thermospheric winds. *Geophysical Research Letters*, *35*(2), L02105. https://doi.org/10.1029/2007GL031522

Vadas, S. L., & Nicolls, M. J. (2009). Temporal evolution of neutral, thermospheric winds and plasma response using PFISR measurements of gravity waves. *Journal of Atmospheric and Solar-Terrestrial Physics*, *71*(6–7), 740–770. https://doi.org/10.1016/j.jastp.2009.01.011

Vadas, S. L., & Nicolls, M. J. (2012). The phases and amplitudes of gravity waves propagating and dissipating in the thermosphere: Theory. *Journal of Geophysical Research*, *117*, A05322. https://doi.org/10.1029/2011JA017426

Vadas, S. L., Xu, S., Yue, J., Bossert, K., Becker, E., & Baumgarten, G. (2019). Characteristics of the quiet-time hotspot gravity waves observed by GOCE over the Southern Andes on 5 July 2010. *Journal of Geophysical Research: Space Physics*, *124*(8), 7034–7061. https://doi.org/10.1029/2019JA026693

Vadas, S. L., Zhao, J., Chu, X., & Becker, E. (2018). The excitation of secondary gravity waves from local body forces: Theory and observation. *Journal of Geophysical Research: Atmospheres*, *123*(17), 9296–9325. https://doi.org/10.1029/2017JD027970

Vierinen, J., Coster, A. J., Rideout, W. C., Erickson, P. J., & Norberg, J. (2016). Statistical framework for estimating GNSS bias. *Atmospheric Measurement Techniques*, *9*(3), 1303–1312. https://doi.org/10.5194/amt-9-1303-2016

Watson, C., Themens, D. R., & Jayachandran, P. T. (2021). Development and validation of precipitation enhanced densities for E-CHAIM. *Space Weather*, *19*(10), e2021SW002779. https://doi.org/10.1029/2021SW002779

Xu, S., Vadas, S. L., & Yue, J. (2021). Thermospheric traveling atmospheric disturbances in austral winter from GOCE and CHAMP. *Journal of Geophysical Research: Space Physics*, *126*(9), e2021JA029335. https://doi.org/10.1029/2021JA029335

Xu, S., Vadas, S. L., & Yue, J. (2024). Quiet time thermospheric gravity waves observed by GOCE and CHAMP. *Journal of Geophysical Research: Space Physics*, *129*(1), e2023JA032078. https://doi.org/10.1029/2023JA032078

Yoshiki, M., & Sato, K. (2000). A statistical study of gravity waves in the polar regions based on operational radiosonde data. *Journal of Geophysical Research*, *105*(D14), 17995–18011. https://doi.org/10.1029/2000jd900204

Zhang, Y., & Paxton, L. J. (2008). An empirical Kp-dependent global auroral model based on TIMED/GUVI data. *Journal of Atmospheric and Solar-Terrestrial Physics*, *70*(8–9), 1231–1242. https://doi.org/10.1016/j.jastp.2008.03.008